

GLASS FORMING ABILITY, MAGNETIC PROPERTIES, AND MECHANICAL
BEHAVIOR OF IRON-BASED AND COBALT-BASED
METALLIC GLASSES

Medha Veligatla

Thesis Prepared for the Degree of
MASTER OF SCIENCE

UNIVERSITY OF NORTH TEXAS

December 2014

APPROVED:

Sundeep Mukherje, Major Professor
Narendra Dahotre, Committee Member
Zhenhai Xia, Committee Member
Samir Aouadi, Committee Member
Nigel Shepherd, Interim Chair of the
Department of Material Science and
Engineering
Costas Tsatsoulis, Dean of the College of
Engineering
Mark Wardell, Dean of the Toulouse Graduate
School

Veligatla, Medha. Glass Forming Ability, Magnetic Properties, and Mechanical Behavior of Iron-Based and Cobalt-Based Metallic Glasses. Master of Science (Material Science and Engineering), December 2014, 75 pp., 9 tables, 28 figures, references, 70 numbered titles.

Lack of crystalline order and microstructural features such as grain/grain-boundary in metallic glasses results in a suite of remarkable attributes including very high strength, close to theoretical elasticity, high corrosion and wear resistance, and soft magnetic properties. In particular, low coercivity and high permeability of iron and cobalt based metallic glass compositions could potentially lead to extensive commercial use as magnetic heads, transformer cores, circuits and magnetic shields.

In the current study, few metallic glass compositions were synthesized by systematically varying the iron and cobalt content. Thermal analysis was done and included the measurement of glass transition temperature, crystallization temperature, and the enthalpies of relaxation and crystallization. Magnetic properties of the alloys were determined including saturation magnetization, coercivity, and Curie temperature. The coercivity was found to decrease and the saturation magnetization was found to increase with the increase in iron content. The trend in thermal stability, thermodynamic properties, and magnetic properties was explained by atomic interactions between the ferromagnetic metals and the metalloids atoms in the amorphous alloys. Mechanical behavior of iron based metallic glasses was evaluated in bulk form as well as in the form of coatings. Iron based amorphous powder was subjected to high power mechanical milling and the structural changes were evaluated as a function of time. Using iron-based amorphous powder precursor, a uniform composite coating was achieved through microwave processing. The hardness, modulus, and wear behavior of the alloys were evaluated using nano-indentation.

Copyright 2014

by

Medha Veligatla

ACKNOWLEDGEMENTS

I would like to express deep gratitude to my advisor, Dr. Sundeep Mukherjee for his support and supervision. I take this privilege to thank him for giving me the opportunity to be a part of his research team. I am grateful to him for believing in me as potential graduate student to pursue research and mentoring me to perform good research in the past two years.

I would like to thank Dr. Narendra Dahotre, Dr. Zhenhai Xia, and Dr. Samir Aouadi for being a part of my committee and adding their valuable suggestions. Extended support from Dr. Yaowu Hao, Associate Professor at University of Arlington and Center for Advanced Research and Technology, University of North Texas by permitting me to utilize laboratory facilities is most appreciated. I will always remember the team projects that I have worked on and would like to thank each and every one from my research group for their help and encouragement.

The moral support from my parents always helped me in accomplishing my goals and I acknowledge them for all my success. Last but not the least, I would like to specially thank Nishita Guntakandla, Dr. Anchal Sondhi, Dr. Shivraj Karewar for their most valued assistance.

TABLE OF CONTENTS

	Page
ACKNOWLEDGEMENTS	iii
LIST OF TABLES	vi
LIST OF FIGURES	vii
CHAPTER 1 INTRODUCTION	1
1.1 Bulk Metallic Glasses (BMGs)	1
1.2 Role of Thermodynamics and Kinetics in Glass Formation	4
1.3 Criteria for Glass Formation	6
1.4 Magnetic Properties	11
1.5 Mechanical Properties	16
1.6 Applications	18
1.7 Thesis Outline	21
CHAPTER 2 EXPERIMENTAL PROCEDURE	23
2.1 Fabrication of Amorphous Ribbons through Melt Spinning	23
2.2 Material Characterization	24
2.3 Vibrating Sample Magnetometry	26
2.4 Mechanical Behavior	27
CHAPTER 3 GLASS FORMING ABILITY OF COBALT AND IRON BASED METALLIC GLASSES	29
3.1 Structure of the Melt Spun Ribbons	29
3.2 Thermodynamic Parameters	30
3.3 Formability and Reduced Glass Transition	34
CHAPTER 4 MAGNETIC PROPERTIES OF COBALT AND IRON BASED METALLIC GLASSES	37

4.1	Saturation Magnetization	37
4.2	Coercivity.....	42
4.3	Thermomagnetic Stability.....	46
4.4	Phases Formed after Crystallization	47
4.5	Metastable Phases	52
CHAPTER 5 MECHANICAL AND WEAR BEHAVIOR OF COBALT AND IRON BASED METALLIC GLASSES		57
5.1	High Energy Mechanical Milling	57
5.2	Iron Based Metallic Glass Coating on Aluminum Substrate	59
5.3	Wear Behavior of Metallic Glass Coating	64
5.4	Hardness and Modulus by Nano-Indentation	66
CHAPTER 6 CONCLUSIONS		69
BIBLIOGRAPHY.....		71

LIST OF TABLES

	Page
Table 1.1	Magnetic properties of iron based and cobalt based metallic glasses.....14
Table 3.1	Calculated atomic size difference, change in mixing enthalpy and change in entropy of mixing.....31
Table 3.2	Calculated PH-S parameter for the alloy system33
Table 3.3	T _g , T _x and ΔT values for the four different alloy compositions34
Table 3.4	Reduced glass transition for the four compositions.....35
Table 4.1	Corresponding saturation magnetization values for the compositions38
Table 4.2	Summarized saturation magnetization values and their corresponding phases51
Table 4.3	Summarized magnetic properties.....56
Table 5.1	Mechanical properties such as hardness and elastic modulus of Co-Fe ribbons ...68

LIST OF FIGURES

	Page
Figure 1.1	Development of metallic glasses in terms of casting thickness2
Figure 1.2	Possible atomic arrangements for the three types of bulk metallic glasses.3
Figure 1.3	TTT curve showing the critical cooling rate required5
Figure 1.4	Classification of magnetic materials as soft, semi-hard, and hard.....12
Figure 1.5	Processed micro sized metallic glass tools.21
Figure 2.1	Differential Scanning Calorimeter set up with reference and sample crucibles.25
Figure 2.2	ADE E5 VSM and schematic representation of VSM set up.26
Figure 2.3	Schematic showing the contact geometry while loading and unloading.27
Figure 3.1	XRD pattern for the amorphous melt spun Co-Fe alloys.29
Figure 4.1	Consolidated M vs H curves for the amorphous melt spun Co-Fe ribbons.38
Figure 4.2	Schematic of DO3 structure of Fe ₃ Si crystal.39
Figure 4.3	Graphical representation of increase in saturation magnetization40
Figure 4.4	Schematic of metal and metalloid random dense packing.....41
Figure 4.5	Graphical representation of effect of iron concentration on coercivity.45
Figure 4.6	Thermomagnetic curves for the four different alloy compositions47
Figure 4.7	SEM micrographs of fully crystallized49
Figure 4.8	M vs H hysteresis curves for fully crystalline samples.....51
Figure 4.9	DSC plot for the composition52
Figure 4.10	M vs H hysteresis curves for the composition53
Figure 4.11	XRD pattern for the composition54
Figure 5.1	XRD pattern for the as received amorphous, 9 hr ball milled, and 12 hr ball milled iron based metallic glass powder.58

Figure 5.2	SEM image and TEM image of 9 hour ball milled iron based metallic glass	59
Figure 5.3	SEM image of iron based metallic glass particles and DSC plot	61
Figure 5.4	EDS elemental distribution of Fe, Mo, Cr, Y, C, and Al across the coating-substrate interface.	62
Figure 5.5	Micrographs: Substrate, microstructure, micrograph, and XRD pattern	63
Figure 5.6	Load vs Displacement curves for the hard and soft phase.....	65
Figure 5.7	Deformation mechanism in metallic glasses.....	67
Figure 5.8	Load vs displacement for the alloys.....	68

CHAPTER 1

INTRODUCTION

1.1 Bulk Metallic Glasses (BMGs)

Bulk metallic glasses are multicomponent metallic alloys with a fully amorphous structure and strong resistance to crystallization. When nucleation and growth are bypassed due to high cooling rates, the liquid atoms are frozen in a random disordered state called glass. [1]. In contrast to crystalline materials, amorphous alloys do not have long range ordering. During equilibrium cooling, thermodynamics plays an important role in the process of crystallization. However, rapid solidification leading to glass formation is a non-equilibrium process, where the kinetics determine the local ordering of atoms [2].

When a liquid transforms to its corresponding crystal, the volume of the liquid decreases discontinuously at the melting temperature, a typical signature of first order phase transformation. However, in case of a metallic glass, the liquid tends to undercool well below its melting temperature and the volume decreases continuously until the liquid falls out of equilibrium at the glass transition temperature.

Figure 1.1 shows the development of metallic glasses since the first report of a binary composition, Au-Si, by Duwez in the year 1960. Starting with thickness as small as 0.01 cm, presently there are various compositions that can be formed to a thickness greater than 10 cm [3]. Using rare earth metals with a combination of other metallic elements, a thickness of 5mm and more was achieved in the year 1989 [4], which extended the use of metallic glasses in commercial applications.

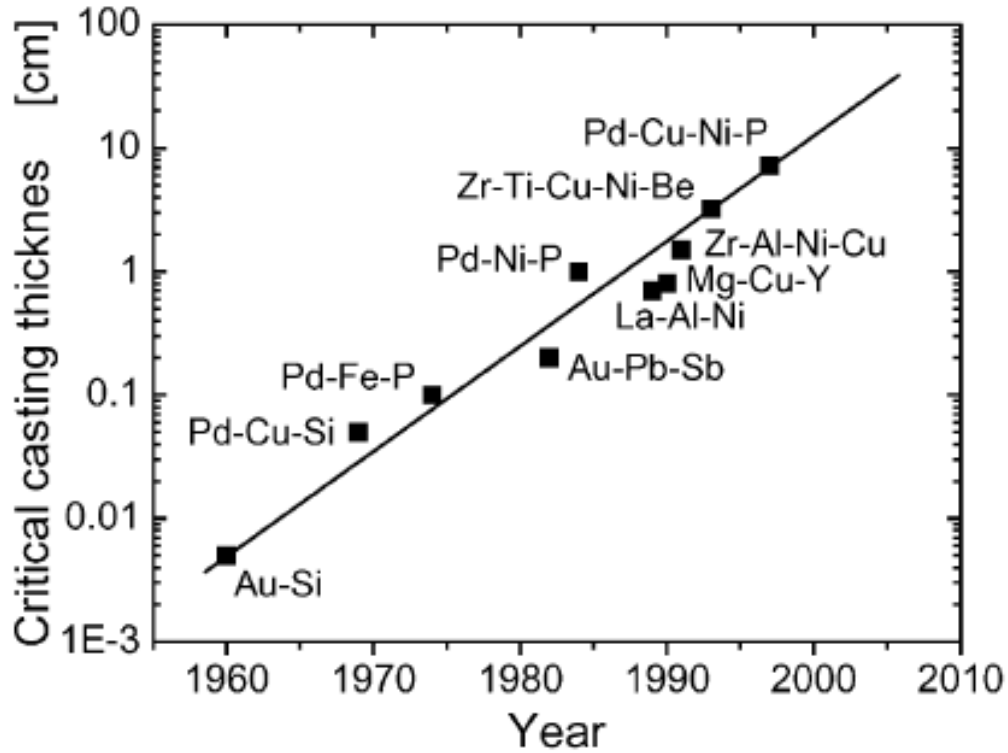


Figure 1.1 Development of metallic glasses in terms of casting thickness as a function of year discovery. [5]

This was followed by development of a Zr – based BMG in 1990's, Vitreloy1 [6] ($\text{Zr}_{41.2}\text{Ti}_{13.8}\text{Cu}_{12.2}\text{Ni}_{10}\text{Be}_{22.5}$) with a critical casting thickness of several centimeters.

BMGs have dense random atomic packing due to the large atomic size difference between its constituents. They lack any form of long range ordering as in crystalline materials. However, they form few local atomic configurations, depending on the type of BMG. Atomic arrangement for the three major types of BMGs that are shown below (figure 1.2): Metal-Metal type, Pd-metalloid type, and metal-metalloid type.

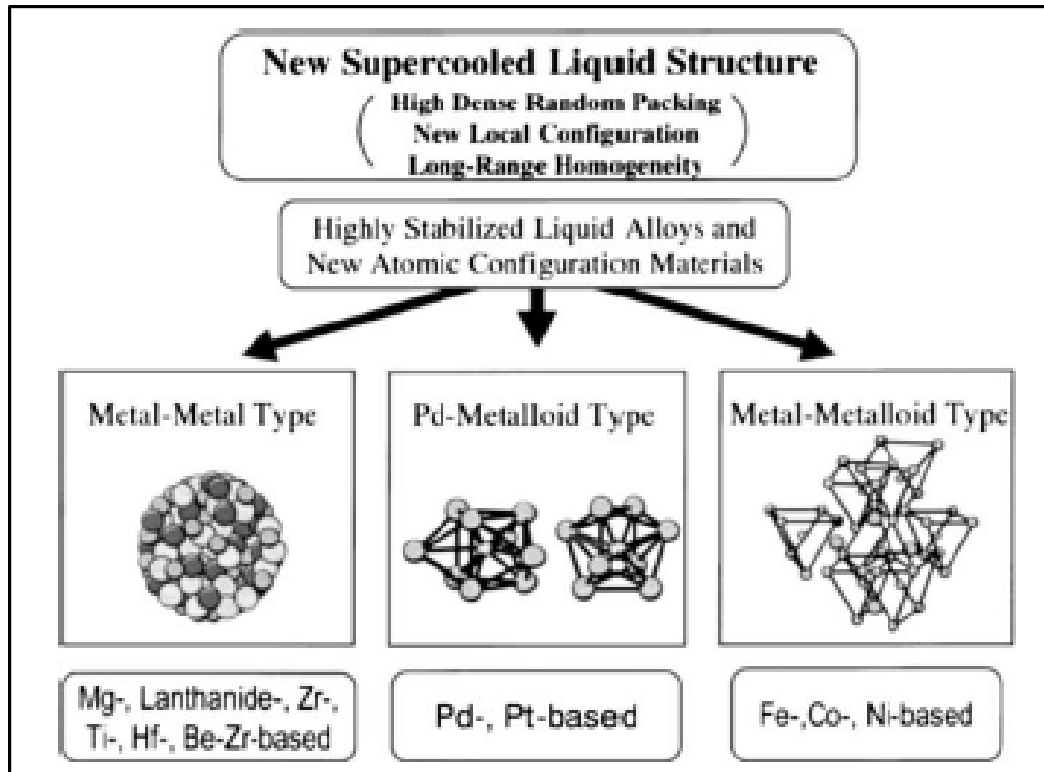


Figure 1.2 Possible atomic arrangements for the three types of bulk metallic glasses [1].

In a metal-metal type of BMG, the atomic arrangement consists of icosahedral clusters, which transform to a quasicrystalline phase (I-phase) during crystallization. Since the I-phase has five fold symmetry, its translational symmetry is incompatible with long range crystalline order. Therefore, it has to dissociate in order to promote the formation of crystalline phases. This discontinuity in transformation suppresses the nucleation and growth process, which leads to high glass forming ability. In case of metal-metalloid type amorphous materials, there is formation of a chain of trigonal prisms connecting larger atoms. The class of BMG that does not follow the typical empirical rules of glass formation is the Pd-based BMG. It consists of trigonal prisms as well as octahedral arrangement of atoms. These two different clusters stabilize the supercooled region.

1.2 Role of Thermodynamics and Kinetics in Glass Formation

A deep understanding of transformation between crystalline and non-crystalline states i.e. solid and liquid state is required to study the role of thermodynamics and kinetics of glass formation. Even with slight undercooling below its melting point, a liquid metal can be maintained in its disordered state without any transformation. In order to promote the solidification process, formation of solid nuclei is necessary. From classical nucleation theory, a critical nuclei radius has to form and the barrier for nucleation of this crystalline nuclei in a liquid is given by

$$\Delta G^* = \frac{16\pi\gamma_{SL}^3}{3(\Delta G_v)^2}$$

where, γ_{SL} is the solid liquid interfacial energy and ΔG_v is free energy associated with the formation of small volume. Therefore upon undercooling, when the clusters in the liquid has a radius greater than the critical radius, the nucleation process starts and the crystalline solid forms. The rate at which this nucleation forms is given by

$$I = \frac{k_n}{n(T)} \exp \left[-\frac{b\alpha^3\beta}{T_r(\Delta T_r)^2} \right]$$

where, b = shape factor, k_n = kinetic constant, $\eta(T)$ = shear viscosity of liquid at temperature T , $T_r = T/T_i$, $\Delta T_r = 1 - T_r$, α and β are dimensionless parameters.

An alloy that can form a glass can be undercooled for sufficiently large time periods. When the critical nucleus size required for crystallization is large, the liquid metal has sufficient time to rearrange its constituent atoms to form a dense packing [7]. Thus, entropy, Gibbs free energy and other thermodynamic parameters can be defined for the metastable liquid state.

Viscosity of the liquid is the kinetic parameter on which the glass formation depends. The motion of the atoms in redistributing itself without forming a nucleus is also termed as diffusivity and from Stokes-Einstein equation, viscosity and diffusivity are related. For avoiding this nucleation/crystallization, a sufficiently high cooling rate is required. This critical cooling rate can be obtained quantitatively from the time – temperature – transformation (T-T-T) curve which gives time until starting of crystallization. The critical cooling rate (R_c) is obtained from the ratio of undercooling to the time at the nose of T-T-T curve. These values vary with composition of the alloy system. The calculated values are 10^{10} Ks^{-1} , 3000 Ks^{-1} and 35 Ks^{-1} for nickel, $\text{Pd}_{82}\text{Si}_{18}$ and $\text{Pd}_{78}\text{Cu}_6\text{Si}_{26}$ respectively [2]. Figure 1.1 is a T-T-T diagram for alloy “a” and alloy “b”. As mentioned above, the liquid needs to be cooled from a temperature above the liquidus temperature to a temperature below the glass transition escaping the nose of the T-T-T curve to solidify into an amorphous structure.

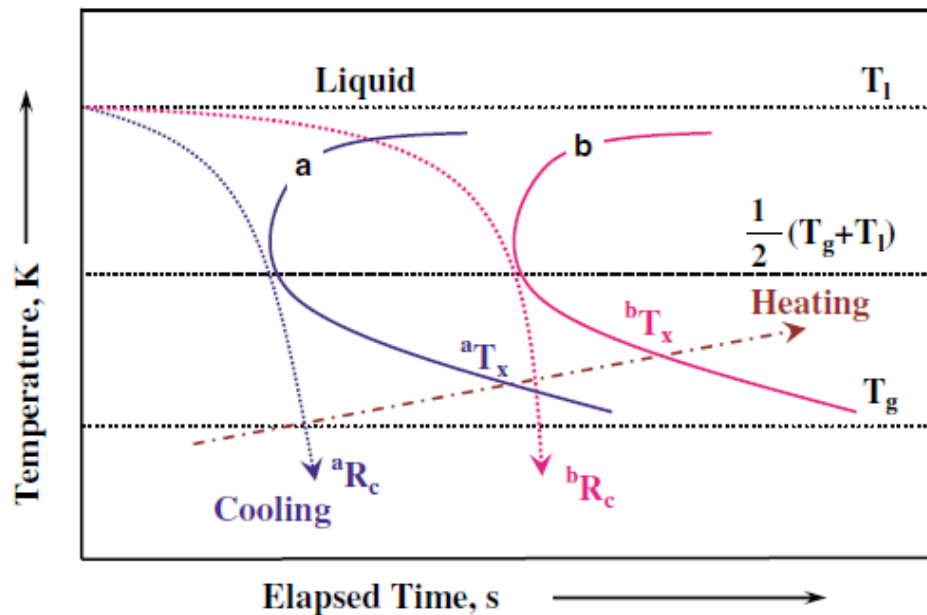


Figure 1.3 TTT curve showing the critical cooling rate required for the alloys “a” and “b” in order to form a glass. [9]

In the example given, alloy “a” has a much higher critical cooling rate (aR_c) compared to alloy “b” (bR_c). Therefore it is easier to vitrify alloy “b” and it is expected to have greater thermal stability compared to alloy “a”. Thus, the GFA of an alloy depends on where the curve lies on the Temperature vs Time plots. Temperature at the nose of the curve, T_n [10] is given by:

$$T_n = \alpha (T_g + T_l)$$

where, $0.45 < \alpha < 0.55$, T_g = glass transition temperature and T_l = liquidus temperature

1.3 Criteria for Glass Formation

1.3.1 Atomic Size Factor

Since the atomic arrangement in a metallic glass is random dense packing, it is likely that the glass forming ability of the alloy is dependent on size of the constituent elements. In the context of relating the size factor and thermodynamics, for an amorphous phase to be stable, Gibbs free energy value of the system must be lowest i.e. the change in Gibbs free energy of the amorphous and crystalline phase must be negative. As Gibbs free energy is given by the equation $G = H - TS$, where H = enthalpy, S = entropy and T = Temperature, either the enthalpy of the system should be low or the entropy needs to be high to keep the free energy of the amorphous state low. The entropy of a system can be increased by increasing the number of components. So, for a multicomponent system with elements of varying atomic size ratios in the range 0.85-1.15 [11], a random dense packing can be achieved.

1.3.2 Effect of Alloying Elements

The position of the T-T-T curve for an alloy is dependent on its composition [12]. With the addition of alloying elements, the T-T-T curve shifts either to the right or left. Curve shift to the left signifies early transformation and shift to the right is a delayed transformation. Therefore, the time required for transformation to occur is affected by alloying addition. Shifting the solid-

liquid transformation curve to the right will retain the liquid state for a longer time, which increases the processing window for BMGs [13]. As the liquid can be maintained in the undercooled state for longer time, the cooling rate for the formation also decreases. Thus, increasing alloy addition in multicomponent system, plays a significant role in lowering the critical cooling rate. Typically, addition of metalloid atoms such as boron, silicon and phosphorous stabilize the liquid and result in better metallic glass forming compositions. This has to do with better packing of the smaller metalloid atoms among the larger metal atoms, which leads to greater stability of liquid.

1.3.3 Deep Eutectic Compositions

An alloy close to a deep eutectic composition is easy to cast into an amorphous structure. The main drawback of this criterion is the availability of phase diagrams for higher order systems (> 2 components). However, there are indirect ways to check if the alloy melts at a single temperature with the help of differential scanning calorimeter and differential thermal analysis. For eutectic compositions, the driving force required for forming crystalline phases is small. Therefore, it becomes easier to bypass crystallization. $\text{Cu}_{50}\text{Zr}_{50}$ [14] is a composition which can form glassy rods about 2mm diameter. But it has been observed that with larger diameters, there is instability of the glassy phases and there is formation of few crystals. By moving a little away from the eutectic composition and adding 4at% Al the crystalline phases can be destabilized, which in turn increase the diameter of the rod to 5mm.

1.3.4 Inoue Criteria

Three empirical rules have been suggested for glass formation by Inoue for

- i. A multicomponent system with at least three alloying elements,
- ii. Atomic size difference of more than 12% among the constituent elements and

- iii. A negative heat of mixing among major constituents of the alloy composition

The first rule comes from basic thermodynamic and kinetic aspects of glass formation. With the advantage of multicomponent system, there is an increase in entropy of fusion which contributes to the stability of the glassy phase. In order to have make the glassy phase stable, the free energy of the glassy phase must be less than the free energy of the corresponding crystalline phase. The increase in entropy of fusion with increasing number of components also contributes to a random dense packing, which lowers the enthalpy of fusion as well. Thus, there is an overall reduction in free energy and the glassy phase remains stable. Contributions from the atomic size difference and negative heat of mixing go towards the random dense packing. This in turn reduces atomic diffusivity and increase the liquid-solid interfacial energy. Therefore, these two criteria also used to explain glass formation [15, 16].

The ΔT_x criteria, also proposed by Inoue, is the most commonly used to quantitatively measure glass forming ability of an alloy composition. ΔT_x is the difference between the crystallization temperature and glass transition temperature. This range is called the supercooled liquid region. Larger the supercooled region, better is the stability of the glassy phase. It has been generalized by Inoue that with increasing ΔT_x for a composition, the critical cooling rate for formation of glass decreases. However there are a few exceptions to this generalization.

$\text{Pd}_{40}\text{Cu}_{30}\text{Ni}_{10}\text{P}_{20}$ [17] and $\text{La}_x\text{Al}_{14}(\text{Cu},\text{Ni})_{86-x}$, $X = 57-70$ at% [18] are two alloy compositions which do not support the ΔT_x criterion. Therefore, the ΔT_x criteria is useful to check for thermal stability rather than glass forming ability.

As discussed earlier, the cooling rate of a specimen varies from its surface to the center. So, the glass forming ability of a composition is limited to the specimen thickness that can be achieved with a specified cooling rate. If an alloy composition has higher glass formability, then

the maximum diameter that it forms in fully amorphous state should also be larger. This maximum thickness that can be achieved increases with decreasing critical cooling rate. The most common method used to produce BMGs with different section thickness at higher solidification rates is the copper wedge mold method. The bulk that is obtained is sliced into sections and these sections are characterized using X-Ray diffraction (XRD) and Transmission Electron Microscopy (TEM). Through this technique the maximum permissible thickness with completely amorphous structure can be determined.

1.3.5 Reduced Glass Transition Temperature

Reduced glass transition temperature is the temperature ratio of glass transition and liquidus temperature. Viscosity of an alloy changes as it is cooled from liquid to solid state. It has been reported that the viscosity of most metallic glasses at glass transition temperature approaches a value of 10^{12} Pas [8]. To form an amorphous phase, homogenous nucleation has to be suppressed. Based on viscosity and crystal nucleation kinetics, reduced glass transition temperature is another parameter used in determining glass forming ability of a system. It is denoted by $T_{rg} = \frac{T_g}{T_l}$. For, a higher value of this ratio the cooling rate required for the formation of a glass will be lower. High glass transition temperature with low liquidus temperature giving a ratio greater than $2/3$ is considered ideal to aid the formation of glass. The smallest value of T_{rg} that still leads to glass formation is 0.4 and the larger it gets the better is its glass forming ability. But having a very large value of T_{rg} is not enough for glass formation, the critical cooling rate also needs to be satisfied. $\text{La}_{55}\text{Al}_{25}\text{Ni}_{20}$ [19], $\text{Ca}_{65}\text{Al}_{35}$ [20], $\text{Pd}_{40}\text{Ni}_{40}\text{P}_{20}$ [21] are few BMGs which have $T_{rg} > 0.65$. However, there are a few binary and ternary systems that are exceptions to this rule. Maximum thickness can also be estimated from T_{rg} when liquidus temperature is used to calculate reduced glass transition. Since the effect of solute concentration is more on liquidus

temperature than glass transition temperature for a binary system, T_{rg} can change dramatically with increase in solute content. Therefore, T_{rg} as a parameter to measure glass forming ability may not be very reliable in all cases.

1.3.6 Miscellaneous Parameters

The amorphous phase stability can be estimated from fundamental properties of the constituent elements. Using the fundamental rules for the formation of solid solution and BMGs, S. Guo et al [22] tried to distinguish HEAs and BMGs. Based on the atomic size difference, mixing enthalpy and entropy of the constituent elements, a solid solution can be set apart from BMG. Formation of a solid solution is possible when the atomic size difference is small with a positive or not very negative mixing enthalpy and high mixing entropy. Whereas, BMGs require negative mixing enthalpies, smaller mixing entropy compared to solid solutions and a larger atomic size difference. Calculating the atomic size difference, enthalpy of mixing and entropy of mixing for equiatomic HEAs and non-equiatomic BMGs, they have obtained a range of values which need to be satisfied for a material to fall in to a category:

Atomic size difference (δ):

$$\delta = 100 \sqrt{\sum_{i=1}^n C_i (1 - r_i/r)^2}$$

where, $r = \sum_{i=1}^n C_i r_i$, C_i = fraction atomic percentage of i^{th} element, r_i = atomic radius of i^{th} element and r = average atomic radius. The alloy composition must have the calculated atomic size difference $\delta \geq 9$ in order to form a BMG.

Enthalpy of mixing (ΔH_{mix}):

$$\Delta H_{mix} = \sum_{i=1, i \neq j}^n \Omega_{ij} C_i C_j$$

here, $\Omega_{ij} = 4 \Delta H_{mix}^{AB}$, C_i, C_j = fraction atomic percentage of i^{th} and j^{th} element respectively

ΔH_{mix}^{AB} is the mixing enthalpy of binary liquid AB alloys. ΔH_{mix}^{AB} for the atomic pairs AB used in calculating enthalpy of mixing were taken from Miedema's model [23]. The acceptable calculated enthalpy of mixing should be in the range of $-49 \leq \Delta H_{mix} \leq -5.5 \text{ KJmol}^{-1}$.

Entropy of mixing (ΔS_{mix}):

$$\Delta S_{mix} = -R \sum_{i=1}^n C_i \ln C_i$$

$R = 8.3144 \text{ JK}^{-1}\text{mol}^{-1}$ and C_i = fraction atomic percentage of i^{th} element

$7 \leq \Delta S_{mix} \leq 16 \text{ JK}^{-1}\text{mol}^{-1}$ is the range for metallic glass formation.

1.4 Magnetic Properties

Numerous compositions of amorphous alloys have been developed over the years. Numerous studies have been done on different alloy systems and it has been observed that the amorphous alloys exhibit exceptionally good electronic, magnetic and mechanical properties due to lack of long range ordering. Of all the metallic alloy systems available, ferromagnetic amorphous alloys are known as the softest magnetic materials available. One main drawback of these alloys is the maximum thickness that can be produced in amorphous form. Since these alloys need very high cooling rates, the thickness of the final product is limited. Amongst the ferromagnetic alloy systems, Fe, Co and Ni base amorphous alloys are being used extensively for magnetic applications. The major use of these magnetic alloys in electrical applications is to maintain a magnetic flux for which high saturation magnetization is needed with low coercivity. Magnetic materials are generally classified as soft and hard magnetic materials depending on their coercivity. The below plot (figure 1.4) shows the distribution of saturation magnetization and coercivity for some commonly used magnetic materials. Coercivity is the measure of

ferromagnetic material that can withstand magnetic field. Materials with coercivity less than 1KA/m are soft magnetic and with coercivity above 50 KA/m are hard magnets [24]. Most of the iron based and cobalt based amorphous alloys are soft magnetic materials.

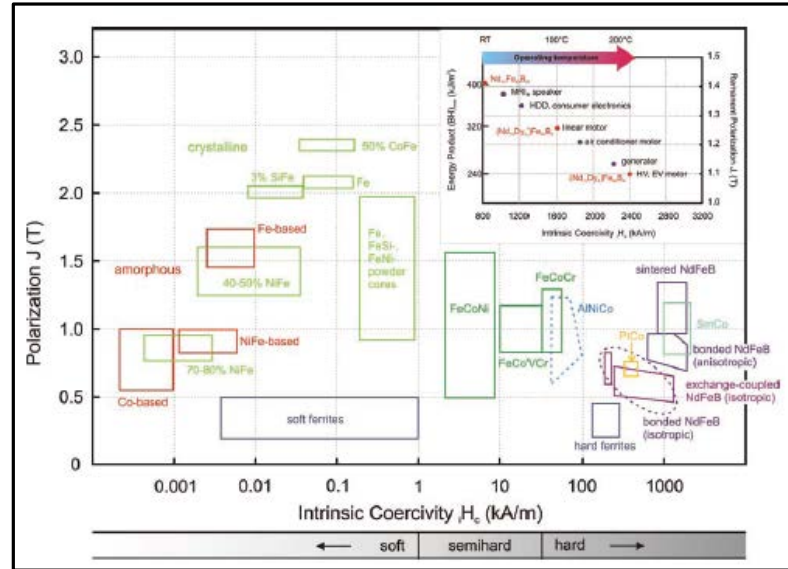


Figure 1.4 Classification of magnetic materials as soft, semi-hard, and hard magnetic materials based on coercivity. [24]

The coercivity of amorphous alloys is sensitive to the thickness of the sample.

Experimentally obtained hysteresis loops for $\text{Nd}_{70}\text{Fe}_{20}\text{Al}_{10}$ [25] of varied thickness show the dependency of coercivity on specimen diameter. Ranging from 30 μm to 5mm thickness, it has been noticed that the ribbon with 30 μm has the lowest coercivity of 5 kA/m when compared to the coercivity of 209 kA/m for 1mm thick sample. This change in coercivity with sample size shows the influence of the material's structure on its magnetic properties. In order to get a sample of maximum thickness, the cooling rate gets compromised which can lead to structural relaxation with increased number of short range ordered structures that increase coercivity.

1.4.1 Iron Based and Cobalt Based Metallic Glasses

Among the different compositions available, iron based BMGs are most favorable for commercial usage. With a combination of excellent soft magnetic properties and high mechanical strength, iron based metallic glasses are best known for commercial usage. $\text{Fe}_{80}\text{P}_{13}\text{C}_7$ [26] is the first amorphous alloy developed with ferromagnetic properties. The choice of metalloid in this alloy is due to its low eutectic temperature with iron. It was observed that the hysteresis curve for this alloys looked very similar to soft ferromagnetic material with 6.8 kG saturation magnetization and 3 Oe coercivity. Melt spun Fe-Si-B amorphous ribbons are also widely studied and used. However, the main drawback is the cooling rate that is required to produce it. Thus, the commercially available Fe-Si-B amorphous alloy used in the transformer cores is only 25 μm thick. In order to have higher magnetization value, the percentage of alloying elements should be kept low. But, in such a case, there might be a compromise on the glass forming ability of the alloy. Therefore, an optimum level of alloying elements are chosen to get a combination of all the properties. Following this observation, an Fe-Si-B-P alloy has been developed with excellent magnetic properties and high GFA. Varying the percentage of Si, B and P, the maximum undercooled region obtained before crystallization is 54K. These ribbons are a combination of low coercivity and high saturation magnetization of 1.51T [27].

Iron based and cobalt based BMGs of the type Fe-(Al, Ga)-(P, C, B, Si, Ge), Fe-TM (TM = IV–VIII group transition metal)-B, Fe(Co)-(Al, Ga)-(P, C, Si, B), Fe-(Co, Ni)-M-B (M = Zr, Hf, Nb, Ta, Mo, W), Fe-Co-Ln-B, Fe-(Nb, Cr, Mo, Ni)-(P, C, B), Co-Fe-(Zr, Hf, Nb)-B are tabulated below along with their magnetic properties (Table1.1).

Table 1.1 Magnetic properties of iron based and cobalt based metallic glasses. [28-45]

Alloy Composition	Thickness (mm)	Saturation Magnetization (T)	Coercivity (A/m)	Curie Temperature (K)
Fe ₈₀ B ₂₀	<0.025	1.65	12	-
Fe ₇₈ Si ₁₃ B ₉	<0.025	1.55	9	-
Fe ₈₀ P ₁₂ B ₄ Si ₄	<0.025	1.13	1.3	-
Fe ₇₆ Si ₉ B ₁₀ P ₅	2.5	1.51	1	-
Fe ₆₂ Nb ₈ B ₃₀	0.035	0.75		516
(Fe _{0.75} B _{0.15} Si _{0.1}) ₉₆ Nb ₄	1.5	1.2	3.7	-
(Fe _{0.75} Si _{0.1} B _{0.15}) ₉₆ Nb ₄	1.5	1.47	2.9	-
Fe ₈₀ Zr ₄ Ti ₃ Cu ₁ B ₁₂	<0.025	0.94	48.5	-
Fe ₇₆ Al ₄ P ₁₂ B ₄ Si ₄	<0.025	1.08	12.7	-
Fe ₇₆ Al ₄ P ₁₂ B ₄ Si ₄	<0.025	1.38	3	623
Fe ₇₆ Mo ₂ Ga ₂ P ₁₀ C ₄ B ₄ Si ₂	2	1.32	3	-
Fe ₇₆ P ₅ (Si _{0.3} B _{0.5} C _{0.2}) ₁₉	3	1.44	1	680
Fe _{37.5} Ni _{22.5} Cr ₅ Co ₁₀ B ₁₅ Si ₁₀	20-25	0.89	3,720	-
Fe ₇₈ Ga ₂ P ₁₂ C ₄ B ₄	0.02	1.34	2	-
Fe ₇₈ Ga ₂ P _{9.5} C ₄ B ₄ Si _{2.5}	2	1.4	3	625
Fe ₇₃ Al ₅ Ga ₂ P ₁₁ C ₅ B ₄	<0.025	1.24	4	-
Fe ₇₄ Al ₄ Ga ₂ P ₁₂ B ₄ Si ₄	<0.025	1.03	19.1	-
Fe ₇₇ Al _{2.14} Ga _{0.86} P _{8.4} C ₅ B ₄ Si _{2.6}	<0.025	1.39	9	-
Fe ₃₀ Co ₃₀ Ni ₁₅ Si ₈ B ₁₇	1.2	0.92	3	-
Fe ₅₆ Co ₇ Ni ₇ Zr ₁₀ B ₂₀	<0.025	0.92		567
Fe ₄₀ Co ₄₀ Cu _{0.5} Al ₂ Zr ₉ Si ₄ B _{4.5}	-	1.18	3	736
Fe ₅₂ Co _{9.5} Nd ₃ Dy _{0.5} B ₃₅	-	1.26	1	-
Fe ₆₂ Co _{9.5} Gd _{3.5} Si ₁₀ B ₁₅	-	0.98	5	596
Fe ₆₂ Co _{9.5} Nd ₃ Dy _{0.5} B ₂₅	-	1.37	4	-
(Fe _{0.85} Co _{0.15}) ₇₇ Ga ₂ P ₁₀ C ₅ B _{3.5} Si _{2.5}	3	1.4	5	694
(Co _{0.0705} Fe _{0.045} Si _{0.1} B _{0.15}) ₉₆ Nb ₄	1	0.59	<3	-
[(Co _{0.6} Fe _{0.4}) _{0.75} B _{0.2} Si _{0.05}] ₉₆ Nb ₄	0.02	-	-	-

$\text{Co}_{43}\text{Fe}_{20}\text{Ta}_{5.5}\text{B}_{31.5}$	0.02	0.51	0.9	-
$\text{Co}_{43}\text{Fe}_{20}\text{Ta}_{5.5}\text{B}_{31.5}$	2	0.49	-	-
$\text{Co}_{43}\text{Fe}_{20}\text{Ta}_{5.5}\text{B}_{31.5}$	3	0.49	0.25	-
$[(\text{Fe}_{0.8}\text{Co}_{0.1}\text{Ni}_{0.1})_{0.75}\text{B}_{0.2}\text{Si}_{0.05}]_{96}\text{Nb}_4$	2.5	1.1	3	-
$[(\text{Fe}_{0.6}\text{Co}_{0.1}\text{Ni}_{0.3})_{0.75}\text{B}_{0.2}\text{Si}_{0.05}]_{96}\text{Nb}_4$	3	0.8	2.5	-
$[(\text{Fe}_{0.6}\text{Co}_{0.2}\text{Ni}_{0.2})_{0.75}\text{B}_{0.2}\text{Si}_{0.05}]_{96}\text{Nb}_4$	4	0.86	2.5	-
$[(\text{Fe}_{0.6}\text{Co}_{0.3}\text{Ni}_{0.1})_{0.75}\text{B}_{0.2}\text{Si}_{0.05}]_{96}\text{Nb}_4$	4	0.9	2	-
$[(\text{Fe}_{0.6}\text{Co}_{0.1}\text{Ni}_{0.1})_{0.75}\text{B}_{0.2}\text{Si}_{0.05}]_{96}\text{Nb}_4$	2.5	1.1	3	-

1.4.2 Effect of Alloying and Annealing on Magnetic Properties

Despite the structure of (crystalline/amorphous) of the alloy, composition plays a vital role in determining the material's saturation magnetization. The increase or decrease of ferromagnetic elements in a composition will directly reflect on the materials magnetic properties. A lot of ferromagnetic alloy systems have been reported with slight changes in composition leading to different magnetic properties. One such alloy is $\text{Fe}_{78}\text{Ga}_2\text{P}_{12}\text{C}_4\text{B}_4$ [42], whose supercooled liquid region increases from 26 K to 50 K and 52 K for $\text{Fe}_{74}\text{Mo}_4\text{Ga}_2\text{P}_{10}\text{C}_4\text{B}_4\text{Si}_2$ and $\text{Fe}_{76}\text{Mo}_2\text{Ga}_2\text{P}_{10}\text{C}_4\text{B}_4\text{Si}_2$ respectively which is obtained by small additions of Mo and Si. Further changing the composition slightly to $\text{Fe}_{73}\text{Mo}_4\text{Ga}_3\text{P}_{10}\text{C}_4\text{B}_4\text{Si}_2$ and $\text{Fe}_{75}\text{Mo}_2\text{Ga}_3\text{P}_{10}\text{C}_4\text{B}_4\text{Si}_2$, ΔT increases to 57 K and 60 K respectively [46]. This increase in supercooled region can be attributed to the changes occurring in the crystallization event. With the addition of Mo and Si, primary crystallization product $(\text{Fe},\text{Mo})_{23}(\text{B},\text{C})_6$, is suppressed which leads to such high values of ΔT . With about 70 at% of ferromagnetic element in the composition and disordered atomic arrangement, they exhibit good soft magnetic properties with a saturation magnetization of 1.11 – 1.32 T and coercivity 2.4 – 3.3 A/m. With the addition of Nb to amorphous Fe-B-Si system an increase in glass forming ability was observed. Addition of 1 at% Nb resulted in a 0.5mm diameter rod, 1mm diameter with 2 at% Nb and 4 at% Nb gave a 1.5mm

diameter rod. The amorphous phase is made more stable with the addition of Nb. With increasing percentage of Nb from 1 at% to 4 at%, the maximum attained saturation magnetization is 1.5T for 1 at% Nb which drops to 1.47T on 4 at% addition of Nb. On the other hand, the coercivity also decreases from 3.7 to 2.9 A/m which makes it more soft magnetic [47].

FINEMET are a class of amorphous alloys which exhibit high saturation magnetization due to formation of ferromagnetic nanocrystalline precipitates on annealing. For the alloys to be able to generate ferromagnetic nanocrystals in an amorphous phase, it is necessary that the alloy undergoes a two stage crystallization. Slight addition of Cu to the alloy Fe-Si-B-Nb has changed the single stage crystallization to a multiple crystallization events [48, 49]. Henceforth, with the advantage of having multiple crystallization peaks, annealing at temperature above the first crystallization event gives fairly competing soft magnetic properties. Upon annealing, irrespective of the crystalline phase forming, the alloys Fe-Co-B-Si-Nb show a decrease in coercivity and increase in permeability keeping the saturation magnetization value more or less the same. Even with the dispersion of α -Fe phase in the amorphous matrix, there is a slight decrease in saturation magnetization when compared to the completely amorphous structure. This reduction in magnetic properties can be attributed to the nonmagnetic elements in the composition.

1.5 Mechanical Properties

Measured mechanical properties of metals lie way below the theoretical values due to the periodicity in atomic arrangement that cause various defects such as dislocations and stacking faults. The absence of such defects in metallic glasses make it possible to achieve exceptionally good mechanical properties that almost reach theoretical limits. Its use in golf heads and tennis racket frames attributes to its high energy storage per unit volume.

BMGs are highly known for their high strength, wear resistance, high hardness, and low coefficient of friction. One such ferromagnetic composition is $\text{Fe}_{50}\text{Cr}_{15}\text{Mo}_{14}\text{C}_{15}\text{B}_6$ which exhibits very high strength with the addition of Y/Ln, the alloy can be cast into a 12mm rod through injection casting method. With 2 at% Y/Ln in the base composition it has attained 13GPa microhardness with 180-200 GPa elastic modulus [50]. A class of iron based metallic glasses, $\text{Fe}_{75}\text{Mo}_5\text{P}_{10}\text{C}_{7.5}\text{B}_{2.5}$ has shown a plastic strain of 5.5% before its failure on a compression test with 1.1 T saturation magnetization and 1.8 A/m coercivity [51]. However, the deformation mechanism in these alloys is inhomogeneous which is attributed to the absence of dislocations. When subjected to a tensile load, BMGs shows a very high yield point with no significant plastic deformation. This type of deformation behavior has been explained with the formation and rapid growth of shear bands that lead to sudden failure of the material. At high strain rates, in contrast to the crystalline materials, strain softening occurs that causes deformation at lower stress values. The shear bands or the localized formation of these shear bands are held responsible for this strain softening behavior. A number of factors contribute to the formation of shear bands such as formation of free volume, localized structural ordering due to shear transformation zone operations, localized heating, and change in internal stresses. These shear band generations have been explained by two mechanisms. One, formation volume that leads to decrease in viscosity reduces density of the material which propagates the deformation mechanism. Other mechanism is localized adiabatic heat generation. Heat generated within the shears bands could lead to increase in temperature above glass transition or up to melting point. This temperature rise lowers the viscosity and thus promotes deformation under applied stress.

It has been observed that serrations occur in load-displacement curves in BMGs during nano-indentation. This serrated flow is obtained when shear bands form and propagate, there is a

sudden drop in load due to which the surrounding material recovers elastically and hinders the shear band growth. Such a repeated process increases free volume within the shears bands which lead to further deformation in the material. Loading rate plays a key role for the generation of serrated flow in the load-displacement curves. It has been observed that serrations become prominent when the loading rates are slow. A sudden rise in the load is termed as *pop-in* and each *pop-in* event corresponds to the generation of individual shear band. However, when the material is subjected to higher loading rates, multiple shear bands are generated simultaneously thus resulting in a smooth load vs displacement curve. The load-displacement curves of Zirconium based and Palladium based BMGs of different compositions also show the dependency of serrated flow on loading rates [52]. As discussed above, the curves obtained with higher loading rates were smooth whereas serrations were observed on the curves subjected to slow loading rates.

1.6 Applications

Bulk metallic glasses are a unique class of materials with exceptionally high strength, excellent soft magnetic properties and thermoplastic processing ability. Bulk metallic glasses are being used in various fields such as such electrical and power generation, electronics, sporting goods, and biomedical applications. A metallic glass composition with low density, low concentration of cytotoxic elements, high fatigue life and high room temperature plasticity can be used as human body implants and also as surgical tools. The most widely used compositions are Ferromagnetic BMGs which are known for their outstanding soft magnetic properties. Few of the soft magnetic applications of BMGs have been discussed in detail.

Magnetic Heads: High saturation with a wide coercivity field along with good wear and corrosion resistance are few of the material properties that are desirable for application in

magnetic heads. The first few cobalt based amorphous alloys showed all of these properties except for wear resistance. Later, reducing the metalloid content by substituting with Niobium, the wear resistance in these alloys showed a considerable improvement. Coercivity which controls the information density of metal tapes can be varied over a wide range by manipulating composition and processing technique used. Electronics industry is another field where the amorphous magnetic ribbons are widely in use. With high electrical resistivity, low hysteresis and eddy current losses the amorphous alloys have replaced most of the crystalline core materials in transformers. A combination of high saturation flux density and low core losses yields a high output power for a transformer. Amorphous FeNi and cobalt alloys showed better output powers than ferrites. Additionally, use of non-magnetostrictive cobalt based amorphous alloys further reduces any losses caused by magnetostrictive vibrations from the core. Amorphous alloys, especially cobalt based with high saturation flux density and permeability are used as spike killers. In many circuits, any sudden change in the current flow can cause electrical noise. Unlike the other noise reducing methods, the amorphous alloys immediately shut down the source of noise. The square shaped hysteresis loop obtained for amorphous alloys is responsible for large inductance when there is no current flow. So, when there is reverse recovery phenomenon in switching devices, the current switches off and because of this there is noise generation in the circuit. Thus, by using amorphous spike killers the noise caused by reverse recovery current is efficiently suspended [53].

Magnetic Sensors and Magnetometers: Amorphous ferromagnetic ribbons and wires that have desirable electrical, magnetic, chemical, and mechanical properties are being used in the production of sensors. There are two types of sensors made from amorphous materials. One is magnetometers with non-magnetostrictive alloys. By altering the curie temperature, these alloys

can be also be used as thermosensors. The other type is stress sensors that are produced using high magnetostrictive alloys [54]. Composition of sensors plays an important role in determining its reliability. The corrosion resistance of iron based amorphous alloys has to be improved by addition of elements that can suppression corrosion. Annealing treatments that alter the microstructure help in improving the sensitivity and temperature stability of sensors. Non-magnetostrictive amorphous sensors are used as magnetic card readers and rotatory encoders. Amorphous alloy sensors are widely being used in computers and information storage devices. Also commercially, use of the amorphous metals is being extended to automobile industries, motors and medical environments.

Besides the applications in magnetic and electric fields, amorphous materials are also used as hard abrasive coatings. Work done by K. Shimamura et al [55] show exceptionally high hardness, corrosion resistance, and high crystallization temperature for sputter coated transition metal amorphous alloys. One such example is sputter coating of Tantalum based amorphous alloy on iron solder tip which improved the life of the tip significantly. Another area where the use of BMGs is extensively being promoted is bio-medical sector.

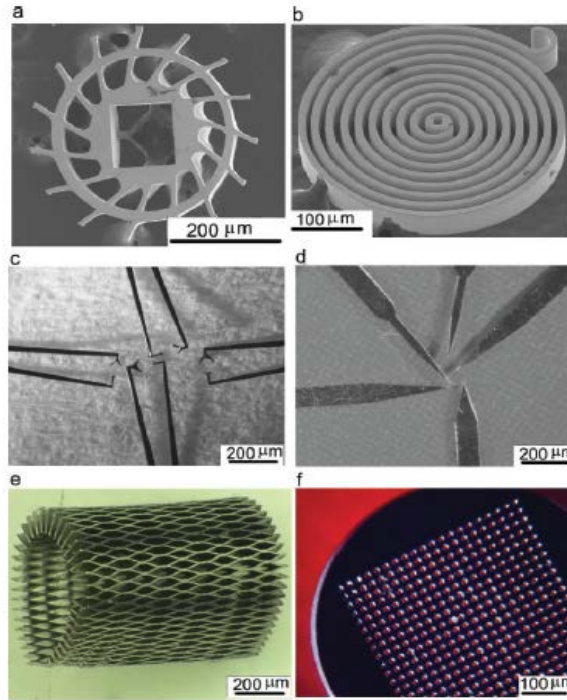


Figure 1.5 Processed micro sized metallic glass tools. [56]

Alloy compositions with mechanical properties similar to body parts, chemically compatible and inert can be used as potential body implants. With high tensile strength and wear resistance, medical tools can also be manufactured. Easy formability of BMGs at low temperatures has further promoted its use in manufacturing micro geared motors. These motors are likely to be used in advanced medical equipment's such as endoscopes, micropumps, precision optics, and many more [2].

1.7 Thesis Outline

In the present study, thermal stability, magnetic properties and mechanical behavior of cobalt and iron based metallic glasses was investigated.

Chapter 1 gives a brief introduction on bulk metallic glasses and the different criteria that are used for its formation. It also introduces some of the Iron based and cobalt based amorphous alloys which are good glass formers with excellent magnetic and mechanical properties. Few of

the applications are discussed in number of different areas of research and technology development.

Chapter 2 contains details on the experimentation section. Instruments that were used in obtaining the results with the details on processing parameters are elaborated.

Chapter 3 comprises of detailed discussion on the thermal stability and microstructural analysis of the four melt spun amorphous alloy compositions $\text{Co}_{72}\text{B}_{19.2}\text{Si}_{4.8}\text{Cr}_4$, $\text{Co}_{64.8}\text{Fe}_{7.2}\text{B}_{19.2}\text{Si}_{4.8}\text{Cr}_4$, $\text{Co}_{57.6}\text{Fe}_{14.4}\text{B}_{19.2}\text{Si}_{4.8}\text{Cr}_4$ and $\text{Co}_{50.4}\text{Fe}_{21.6}\text{B}_{21.6}\text{Si}_{4.8}\text{Cr}_4$. Also, the influence of iron content on glass forming ability is discussed.

Chapter 4 includes the evaluation the magnetic properties of amorphous as well as crystalline $\text{Co}_{72}\text{B}_{19.2}\text{Si}_{4.8}\text{Cr}_4$, $\text{Co}_{64.8}\text{Fe}_{7.2}\text{B}_{19.2}\text{Si}_{4.8}\text{Cr}_4$, $\text{Co}_{57.6}\text{Fe}_{14.4}\text{B}_{19.2}\text{Si}_{4.8}\text{Cr}_4$ and $\text{Co}_{50.4}\text{Fe}_{21.6}\text{B}_{21.6}\text{Si}_{4.8}\text{Cr}_4$ ribbons using a wide range of equipment. The influence of increasing iron content on saturation magnetization is discussed. A comparison of M vs H curves for the four amorphous melt spun alloys and its crystallized samples was done. The coercivity values for the amorphous and crystalline samples is reported and also its trend with the percentage of iron in the composition is reported. The magnetic properties of the samples were also tested as a function of temperature and the curie temperatures were determined. The thermomagnetic results have been graphically reported and the explained with the help of phase analysis from the X-Ray diffraction patterns.

In Chapter 5 the mechanical behavior of amorphous alloys is reported. The wear resistance and hardness of the samples were evaluated with tribometer and nanoindenter respectively. The trend in hardness and resistance to wear as a function of percentage of iron is discussed.

Chapter 6 summarizes the thesis from results and discussions that were obtained.

CHAPTER 2

EXPERIMENTAL PROCEDURE

2.1 Fabrication of Amorphous Ribbons through Melt Spinning

In order to keep the alloy in an amorphous state, the size and thickness of the sample is limited to ribbons. Melt spinning is the most commonly adapted technique to fabricate amorphous ribbons.. The width of the ribbon could vary from a few millimeters to microns scale and the thickness is fixed to micron scale. A good judgment of elemental constituents of the alloys with appropriate cooling rate is necessary to obtain an amorphous alloy with desired properties.

Fe, Co, B, Si and Cr 99.9% pure in elemental form were melted in an arc furnace. The alloys were re-melted 3 times in argon atmosphere in order to make sure that the melt was consistent and to keep it free from oxidation. Maintaining the speed (), the molten mixture is let to flow on to the copper wheel. With the wheel continuously rotating, ribbons of 30 - 40 μ m thickness were produced that are 3mm wide. Ribbons of four different compositions have been fabricated by substituting 7.2 at% of cobalt from each alloy with iron. $\text{Co}_{72}\text{B}_{19.2}\text{Si}_{4.8}\text{Cr}_4$ is the composition of one of the four ribbons which does not contain any iron. Replacing 7.2 at% of cobalt from this alloy with iron we obtained $\text{Co}_{64.8}\text{Fe}_{7.2}\text{B}_{19.2}\text{Si}_{4.8}\text{Cr}_4$. By subsequently adding 7.2 at% iron with cobalt to the existing composition the other two compositions, $\text{Co}_{57.6}\text{Fe}_{14.4}\text{B}_{19.2}\text{Si}_{4.8}\text{Cr}_4$ and $\text{Co}_{50.4}\text{Fe}_{21.6}\text{B}_{19.4}\text{Si}_{4.8}\text{Cr}_4$ are also fabricated. The ribbons thus produced are shiny and lustrous with dimensional similarity.

2.2 Material Characterization

2.2.1 X-Ray Diffractometry and Phase Analysis

The atomic arrangement of an amorphous system is random packing of elemental constituents. However, it undergoes some short range ordering identical to Bernal polyhedral with the transition metal elements on the corners and metalloids residing in the center of the structure. X-ray diffraction is the most commonly used technique to confirm the glassy structure of a material. The presence of a broad hump confirms the amorphous structure of the alloy. A fourier transformation of this data give atomic pair correlation functions. These functions declare the presence of transition metal – metalloid and transition – transition metal pair and no metalloid – metalloid pair which upholds the justification to dense random packing of amorphous alloys. Thus we use X-Ray diffractometry, a non-destructive way to confirm the amorphous structure of the composition.

The four different melt spun compositions and four crystallized ribbons were characterized with Rigaku III Ultima X-Ray Diffractometer. The surface of the ribbons were mechanically polished on a 1200 grit SiC paper in order to get rid of any oxide layer. The X-Ray source used in obtaining the diffraction pattern is Cu K_{α} radiation of wavelength 1.54\AA . The operating voltage and current were 40kV and 44mA. The 2θ range within which the patterns were obtained was 20° - 90° with a scanning rate of $1^{\circ}/\text{min}$ and 0.2° step size. Processing of the obtained diffraction patterns was done using the industry standard software Jade9.

2.2.2 Microstructural Analysis with Scanning Electron Microscopy

The amorphous and the crystalline ribbons were cut and mechanically polished for its microstructural analysis. The samples were polished on 1200 grit SiC papers followed by final polishing with diamond suspension (1μ particle size) and colloidal silica suspension (0.05μ

particle size) for SEM studies. Then polished samples were cleaned with organic soap solution followed by distilled water, methanol and ethanol for 5min in an ultrasonicator. Backscattered images were acquired at an operating voltage range of 15-20kV using the FEI Quanta ESEM - field emission gun SEM.

2.2.3 Differential Scanning Calorimetry

Thermal analysis of the melt spun amorphous ribbons was done with the help of a high temperature differential scanning calorimeter, model- NETZSCH STA 449 F3. A small part of the ribbon cut and ultrasonicated in methanol for 10mins. About 2mg of the cleaned sample is weighed and placed in alumina crucible.

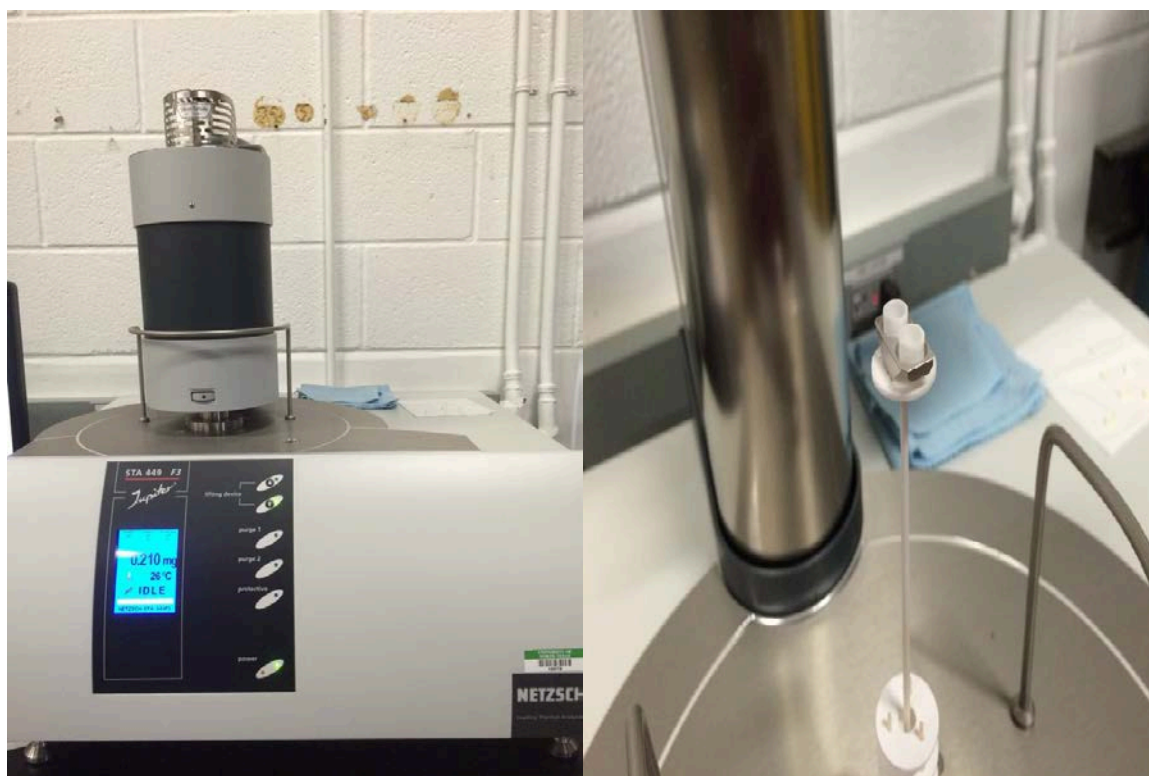


Figure 2.1 Differential Scanning Calorimeter set up with reference and sample crucibles.

The reference crucible used is an empty alumina crucible. The sample is then placed in operating conditions with a heating rate of 20K/min in an Argon atmosphere. The samples were heated from 470K to 970K. This heating cycle was performed twice and the sample was furnace

cooled to room temperature. A plot between DSC signal in (mW/g) and temperature within the heating cycle shows the transition from an amorphous to a crystalline phase.

2.3 Vibrating Sample Magnetometry

Using the ADE E5 Vibrating sample magnetometer the M vs H hysteresis curves were obtained for the ferromagnetic amorphous as well as the crystalline ribbons. Before the measurement starts, the instrument is calibrated with a standard, nickel. Samples were cut in square shape weighing about 1.5mg and thoroughly cleaned with methanol. The sample is attached to a nonmagnetic probe with the help of a parafilm tape and suspended between the two electromagnets. The sample is placed such that it is at the center of the two electromagnets. The purpose of the loudspeaker cone is to vibrate the sample within the electromagnets with a known frequency.

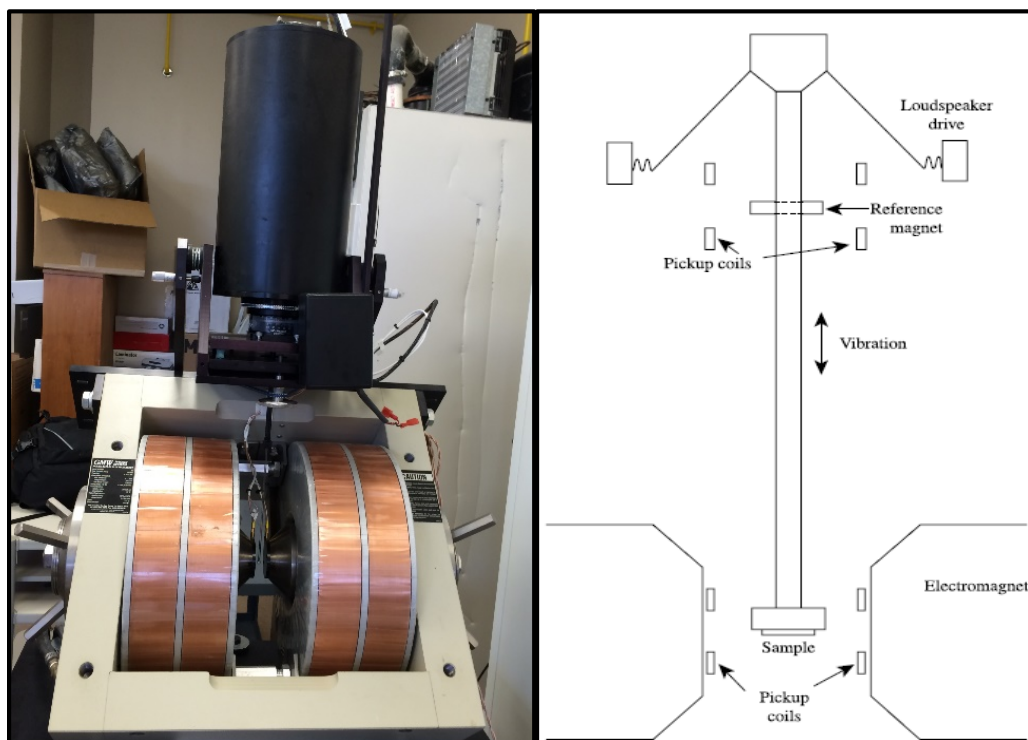


Figure 2.2 ADE E5 VSM and schematic representation of VSM set up.

The above shown schematic is the most commonly used VSM operating set up.

Depending on the mass of the sample and its interaction with the magnetic field, the amplitude of frequency of vibration will vary. A complete loop of the hysteresis curve has been obtained with a maximum applied field of 800000A/m.

2.4 Mechanical Behavior

Instrumented nano-indentation has been performed on bulk metallic glass samples in order to achieve small scale estimation of their mechanical characteristics. The need to image the deformed areas has been eliminated by simple estimation of materials mechanical behavior from its load vs displacement curves. Small scale experimentation makes it more feasible for measuring the hardness and modulus for thin films and micro scale specimens. The unloading path in figure 2.3 is chosen to explain the measurement of hardness and elastic modulus where h_f is the permanent depth of indentation that remains even after unloading. The berkovich indenter is assumed to be equivalent to that of a conical that gives the same depth-area relation with $\phi = 70.3^\circ$ [57].

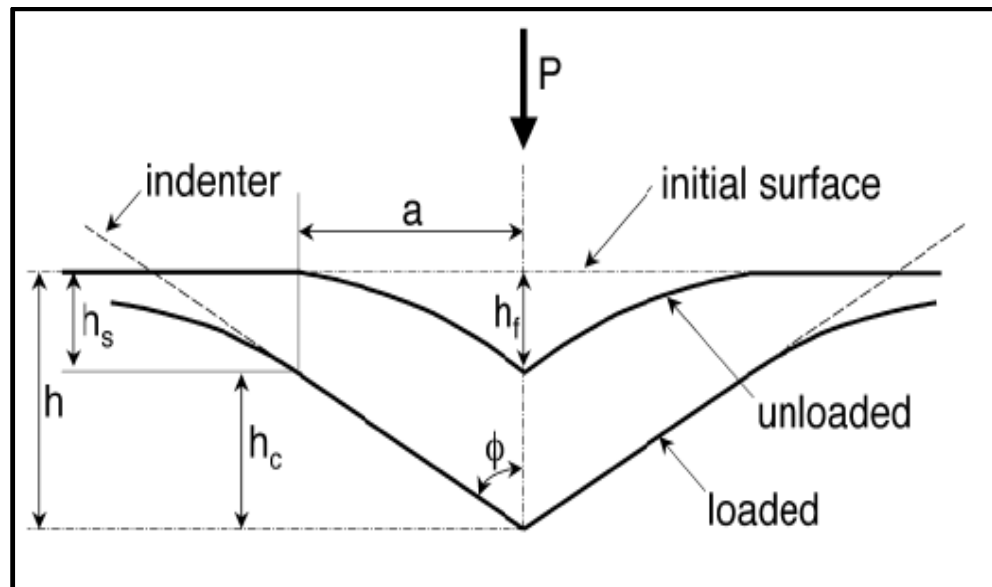


Figure 2.3 Schematic showing the contact geometry while loading and unloading. [57]

Load – displacement curves were generated to obtain hardness and elastic modulus for iron based coating and bulk forms of amorphous materials with a standard Berkovich indenter with a peak load of 7000 μN .

To further evaluation of the wear resistance was done for which scratch tests were conducted. The relative volume loss in the material was also calculated. A universal tribometer (RTEC Instruments) with a 6 mm ceramic ball at constant normal load of 100 N was used to perform scratch tests on the iron BMG coating sample. Velocity was kept constant at 0.03 mm/s for a scratch length of 1 mm spanning across the desired area. With the help of a profilometer, scratch depth at different locations and wear volume loss were estimated.

CHAPTER 3

GLASS FORMING ABILITY OF COBALT AND IRON BASED METALLIC GLASSES

3.1 Structure of the Melt Spun Ribbons

The four alloy compositions which satisfy the fundamental principles of glass formations, $\text{Co}_{72}\text{B}_{19.2}\text{Si}_{4.8}\text{Cr}_4$, $\text{Co}_{64.8}\text{Fe}_{7.2}\text{B}_{19.2}\text{Si}_{4.8}\text{Cr}_4$, $\text{Co}_{57.6}\text{Fe}_{14.4}\text{B}_{19.2}\text{Si}_{4.8}\text{Cr}_4$ and $\text{Co}_{50.4}\text{Fe}_{21.6}\text{B}_{19.2}\text{Si}_{4.8}\text{Cr}_4$ have been produced via melt spinning technique. The ribbons thus obtained have a lustrous surface finish with a thickness of 30 - 40 μm .

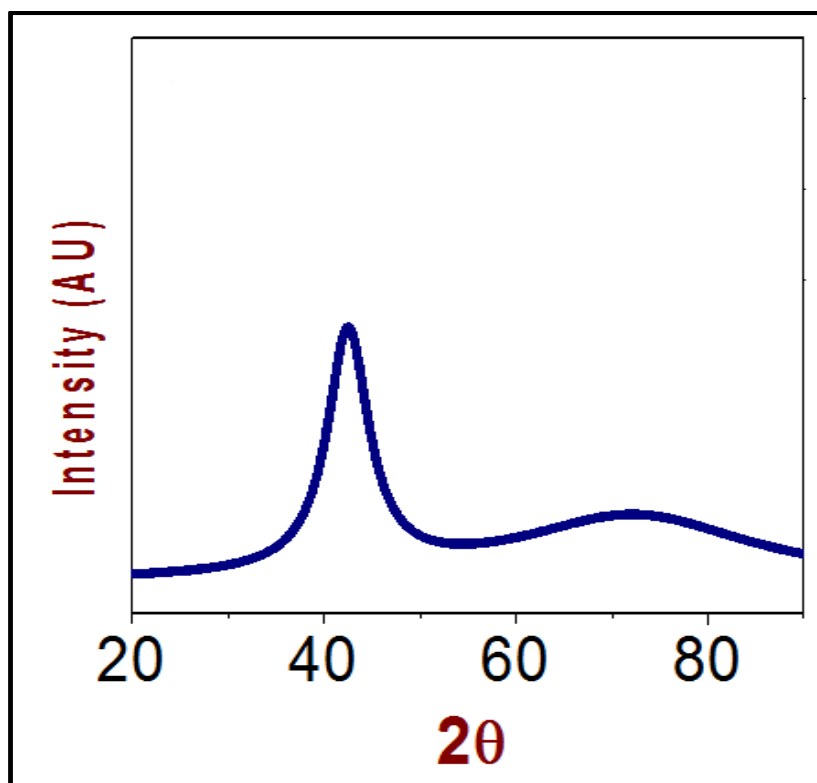


Figure 3.1 XRD pattern for the amorphous melt spun Co-Fe alloys.

To make sure that the composition has a uniform amorphous structure XRD was done on these ribbons. Figure 3.1 shows the obtained XRD pattern for the four melt spun compositions. A broad pattern with the absence of crystalline peaks confirm the amorphous structure with a

random atomic arrangement. All the four compositions show similar XRD pattern as that in figure3.1.

3.2 Thermodynamic Parameters

Composition of the alloy system that is being studied is $[(Co_{(1-X)}Fe_{(X)}) (0.75) B(0.2) Si(0.05)]96 Cr_{(4)}$ where $X = 0, 0.1, 0.2$ and 0.3 . The four alloys have been fabricated by melt spinning process and their corresponding compositions are $Co_{72}B_{19.2}Si_{4.8}Cr_4$, $Co_{64.8}Fe_{7.2}B_{19.2}Si_{4.8}Cr_4$, $Co_{57.6}Fe_{14.4}B_{19.2}Si_{4.8}Cr_4$ and $Co_{50.4}Fe_{21.6}B_{19.2}Si_{4.8}Cr_4$ that are formed by substituting Co with increments of 7.2 at% Fe.

As the high entropy alloys have merged as multi-component single phase solid solutions which are similar to that of bulk metallic glasses, we need to know the type of phases that can evolve from a particular composition and make sure that the stability of the amorphous phase to form BMGs. Though this is challenging there are few fundamental rules that distinguish between BMG and HEA [22]. In order to form the amorphous ribbons through melt spinning process, it is first necessary to check if the desired compositions falls into the category of bulk metallic glasses. The three empirical rules that Inoue had proposed for BMGs must be satisfied and they are large atomic size difference, smaller negative enthalpy and entropy of mixing. Based on these fundamental rules, Zhang et al had chosen three parameters, atomic size difference (δ), mixing enthalpy (ΔH_{mix}) and mixing entropy (ΔS_{mix}) to statistically classify the multi component systems into BMGs and HEAs. With the help of the following three equations

$$\delta = 100 \sqrt{\sum_{i=1}^n C_i (1 - r_i/r)^2} \quad (2)$$

$$r = \sum_{i=1}^n C_i r_i$$

where, C_i = fraction atomic percentage of i^{th} element, r_i = atomic radius of i^{th} element ($\text{Co} = 1.251 \text{ \AA}$, $\text{Fe} = 1.241 \text{ \AA}$, $\text{B} = 0.820 \text{ \AA}$, $\text{Cr} = 1.24 \text{ \AA}$, $\text{Si} = 1.153 \text{ \AA}$) and r = average atomic radius

$$\Delta H_{mix} = \sum_{i=1, i \neq j}^n \Omega_{ij} C_i C_j \quad (3)$$

$\Omega_{ij} = 4 \Delta H_{mix}^{AB}$, ΔH_{mix}^{AB} is the mixing enthalpy of binary liquid AB alloys. ΔH_{mix}^{AB} for the atomic pairs AB used in calculating enthalpy of mixing were taken from Miedema's model[58].

$$\Delta S_{mix} = -R \sum_{i=1}^n C_i \ln C_i \quad (4)$$

where $R = 8.3144 \text{ JK}^{-1}\text{mol}^{-1}$

Table 3.1 Calculated atomic size difference(δ), change in mixing enthalpy ($[\Delta H]_{mix}$) and change in entropy of mixing (ΔS_{mix}).

Composition	δ	$\Delta H_{mix} \text{ (KJmol}^{-1}\text{)}$	$\Delta S_{mix} \text{ (JK}^{-1}\text{mol}^{-1}\text{)}$
$\text{Co}_{72}\text{B}_{19.2}\text{Si}_{4.8}\text{Cr}_4$	9.9	-20.737536	6.883345994
$\text{Co}_{64.8}\text{Fe}_{7.2}\text{B}_{19.2}\text{Si}_{4.8}\text{Cr}_4$	9.9	-20.95872	8.829412303
$\text{Co}_{57.6}\text{Fe}_{14.4}\text{B}_{19.2}\text{Si}_{4.8}\text{Cr}_4$	9.8	-21.138432	9.878939049
$\text{Co}_{50.4}\text{Fe}_{21.6}\text{B}_{19.2}\text{Si}_{4.8}\text{Cr}_4$	9.8	-21.276672	10.5402045

From the calculated values in the above table, the atomic size difference and enthalpy of mixing for the four alloy compositions is approximately 10 and -21 KJmol^{-1} respectively. The mixing entropy falls in the range 7-10 $\text{JK}^{-1}\text{mol}^{-1}$. Thus the calculated values of atomic size difference and enthalpy and entropy heats of mixing are in good accordance with the given range for BMGs, $\delta \geq 9$, $-49 \leq \Delta H_{mix} \leq -5.5 \text{ KJmol}^{-1}$ and $7 \leq \Delta S_{mix} \leq 16 \text{ JK}^{-1}\text{mol}^{-1}$. Having satisfied the statistical limits, these compositions have been selected to be fabricated as amorphous ribbons.

3.2.1 P_{H-S} Parameter

Since there are a few alloy systems whose glass forming ability does not follow the ΔT criteria, the P_{H-S} parameter [23] was also calculated for the four compositions. Using thermodynamic and topological models, we try to relate the glass forming ability of the four alloy compositions to P_{H-S} parameter.

$$P_{H-S} = \Delta H^{chem} \left(S_{\sigma} / K_B \right) \quad (5)$$

Here ΔH^{chem} is the enthalpy of chemical mixing given by

$$\begin{aligned} \Delta H^{chem} = & \Delta H_{Fe-Co}^c + \Delta H_{Fe-B}^c + \Delta H_{Fe-Si}^c + \Delta H_{Fe-Cr}^c + \Delta H_{Co-B}^c \Delta H_{Co-Si}^c + \Delta H_{Co-B}^c + \\ & \Delta H_{Co-Cr}^c + \Delta H_{B-Si}^c + \Delta H_{B-Cr}^c \end{aligned} \quad (6)$$

ΔH_{i-j}^c is the interaction between the elements which is given by

$$\Delta H_{i-j}^c = x_i x_j (x_i \Delta H_{i-j}^{mix} + x_j \Delta H_{j-i}^{mix}), \quad (7)$$

ΔH_{i-j}^{mix} and $x_i \Delta H_{j-i}^{mix}$ are the enthalpies of mixing of *i*th element in *j*th solvent and *j*th element in *i*th solvent respectively. The values enthalpy of mixing for the atomic pairs Fe-Co, Fe-B, Fe-Si, Fe-Cr, Co-B, Co-Si, Co-B, Co-Cr, B-Si and B-Cr have were taken from Miedema's model.

S_{σ} is termed as mismatch entropy which comes with the effect of atomic size difference, also termed as mismatch entropy. From the thermodynamic concepts of mixing of hard spheres, the S_{σ} term is the solution of the Perkus-Yevik integral equation. (Mansoori et al) which is calculated as a function of atomic diameter, composition and packing fraction.

$$S_{\sigma} = k_B \left[\frac{3}{2} (\zeta^2 - 1) y_1 + \frac{3}{2} (\zeta^2 - 1)^2 y_2 - \left\{ \frac{1}{2} (\zeta - 1)(\zeta - 3) + \ln \zeta \right\} (1 - y_3) \right] \quad (8)$$

k_B = Boltzmann constant,

$\zeta = 1/(1 - \xi)$, where $\xi = 0.64$, packing factor for a dense random packing

$$y_1 = \frac{1}{\sigma^3} \sum_{j>i=1}^3 (d_i - d_j)(d_i - d_j)^2 c_i c_j, \quad (9)$$

$$y_2 = \frac{\sigma^2}{(\sigma^3)^2} \sum_{j>i=1}^3 d_i d_j (d_i - d_j)^2 c_i c_j, \quad (10)$$

$$y_3 = \frac{(\sigma^2)^3}{(\sigma^3)^2}, \text{ and} \quad (11)$$

$$\sigma^k = \sum_{i=1}^3 c_i d_i^k, \quad (12)$$

d_i is the atomic diameter of i th element.

The calculated P_{H-S} parameter for the four different compositions has been calculated and tabulated as follows.

Table 3.2 Calculated PH-S parameter for the alloy system $[\{Co(1-X)Fe(X)\}(0.75)B(0.2)Si(0.05)]_{96}Cr_4$ where, $X = 0, 0.1, 0.2 \text{ \& } 0.3$.

Composition	Iron Content (at%)	P_{H-S} parameter
$Co_{72}B_{19.2}Si_{4.8}Cr_4$	0	-23.81179
$Co_{64.8}Fe_{7.2}B_{19.2}Si_{4.8}Cr_4$	7.2	-19.48412
$Co_{57.6}Fe_{14.4}B_{19.2}Si_{4.8}Cr_4$	14.4	-14.23563
$Co_{50.4}Fe_{21.6}B_{19.2}Si_{4.8}Cr_4$	21.6	-14.00031

The P_{H-S} parameter has been used to correlate with the glass forming ability. The alloy systems for which the P_{H-S} parameter has been previously correlated to glass forming ability are Cu-Zr-Al, Cu-Ti-Zr and Fe-Zr-B-Cu. For the present alloy system, $[\{Co_{(1-X)}Fe_{(X)}\}(0.75)B(0.2)Si(0.05)]_{96}Cr_{(4)}$, the P_{H-S} parameter shows a drop in value with increasing iron in the composition. Since the glass forming ability is the measure of maximum thickness that can be obtained for a particular composition, taking the P_{H-S} as the basis, amongst the four alloy

compositions listed in Table 3.2, there is a possibility that the two alloys $\text{Co}_{57.6}\text{Fe}_{14.4}\text{B}_{19.2}\text{Si}_{4.8}\text{Cr}_4$ and $\text{Co}_{50.4}\text{Fe}_{21.6}\text{B}_{19.2}\text{Si}_{4.8}\text{Cr}_4$ can be extended to bulk fabrication.

3.3 Formability and Reduced Glass Transition

3.3.1 ΔT criteria – Glass Forming Ability

Table 3.3 T_g , T_x and ΔT values for the four different alloy compositions with varying iron concentration.

Composition	Percentage of iron (at%)	T_g (K)	T_x (K)	ΔT (K)
$\text{Co}_{72}\text{B}_{19.2}\text{Si}_{4.8}\text{Cr}_4$	0	743.1	792.4	49.3
$\text{Co}_{64.8}\text{Fe}_{7.2}\text{B}_{19.2}\text{Si}_{4.8}\text{Cr}_4$	7.2	756.6	800.2	43.6
$\text{Co}_{57.6}\text{Fe}_{14.4}\text{B}_{19.2}\text{Si}_{4.8}\text{Cr}_4$	14.4	747.6	827.3	79.7
$\text{Co}_{50.4}\text{Fe}_{21.6}\text{B}_{19.2}\text{Si}_{4.8}\text{Cr}_4$	21.6	759.9	807.5	47.6

Another interesting observation is that, with increasing the iron concentration in the composition, there is a shift in the glass transition temperature. There is a clear shift in glass transition temperature and crystallization temperature for the alloys containing 7.2 at% and 21.6 at% iron to higher temperatures when compared to the alloy with 0 at% iron. However, the ΔT for these three alloys remains approximately the same. Being the best glass former among the four alloys with a wide supercooled liquid region, the glass transition and crystallization temperature of $\text{Co}_{57.6}\text{Fe}_{14.4}\text{B}_{19.2}\text{Si}_{4.8}\text{Cr}_4$ deviates from the trend followed by rest of the alloys.

3.3.2 Reduced Glass Transition $\left(T_g/T_l\right)$ Parameter

Reduced glass transition denoted by T_{rg} is the ratio of glass transition temperature and melting temperature. To form a glassy alloy, molten metal is brought down to a temperature below its glass transition by incorporating very high cooling rates. As the molten metal solidifies, the viscosity of the material reaches a very high value. For most of the alloys, viscosity at glass

transition temperature remains constant ($\sim 10^{12}$ Pa s). Therefore, on the basis of crystallization kinetics and viscosity of melts, the ratio of glass transition temperature to the melting temperature is considered as one of the parameters to measure glass forming ability. The higher the reduced glass transition values, better is the glass forming ability of the composition. In other words, any composition having a high glass transition temperature and low melting point can form a glass at reasonably low cooling rates. With a value of T_{rg} less than 0.4, the alloy cannot promote glass formation. Melting point represent by T_l is the liquidus temperature. The temperature where melting ends is taken as the liquidus temperature. The T_{rg} values for the four amorphous compositions $\text{Co}_{72}\text{B}_{19.2}\text{Si}_{4.8}\text{Cr}_4$, $\text{Co}_{64.8}\text{Fe}_{7.2}\text{B}_{19.2}\text{Si}_{4.8}\text{Cr}_4$, $\text{Co}_{57.6}\text{Fe}_{14.4}\text{B}_{19.2}\text{Si}_{4.8}\text{Cr}_4$ and $\text{Co}_{50.4}\text{Fe}_{21.6}\text{B}_{19.2}\text{Si}_{4.8}\text{Cr}_4$ is summarized in Table4. All the alloys show similar values and also above 0.4 indicating that they are good glass formers.

Table 3.4 Reduced glass transition for the four compositions $\text{Co}_{72}\text{B}_{19.2}\text{Si}_{4.8}\text{Cr}_4$, $\text{Co}_{64.8}\text{Fe}_{7.2}\text{B}_{19.2}\text{Si}_{4.8}\text{Cr}_4$, $\text{Co}_{57.6}\text{Fe}_{14.4}\text{B}_{19.2}\text{Si}_{4.8}\text{Cr}_4$ and $\text{Co}_{50.4}\text{Fe}_{21.6}\text{B}_{19.2}\text{Si}_{4.8}\text{Cr}_4$.

Composition	Percentage of iron (at%)	T_g (K)	T_l (K)	$\left(T_g/T_l\right)$
$\text{Co}_{72}\text{B}_{19.2}\text{Si}_{4.8}\text{Cr}_4$	0	743.1	1380.7	0.538
$\text{Co}_{64.8}\text{Fe}_{7.2}\text{B}_{19.2}\text{Si}_{4.8}\text{Cr}_4$	7.2	756.6	1370	0.552
$\text{Co}_{57.6}\text{Fe}_{14.4}\text{B}_{19.2}\text{Si}_{4.8}\text{Cr}_4$	14.4	747.6	1376.2	0.543
$\text{Co}_{50.4}\text{Fe}_{21.6}\text{B}_{19.2}\text{Si}_{4.8}\text{Cr}_4$	21.6	759.9	1379.1	0.551

From the DSC plots (not shown here), the end point of melting event was considered as liquidus temperature which were found to be 1380.7K, 1370K, 1376.2K, and 1379.1K for $\text{Co}_{72}\text{B}_{19.2}\text{Si}_{4.8}\text{Cr}_4$, $\text{Co}_{64.8}\text{Fe}_{7.2}\text{B}_{19.2}\text{Si}_{4.8}\text{Cr}_4$, $\text{Co}_{57.6}\text{Fe}_{14.4}\text{B}_{19.2}\text{Si}_{4.8}\text{Cr}_4$, and $\text{Co}_{50.4}\text{Fe}_{21.6}\text{B}_{19.2}\text{Si}_{4.8}\text{Cr}_4$ compositions respectively. The reduced glass transition ratio for the four compositions falls in the range 0.52 - 0.55. As we know that reduced glass transition temperature is a measure of glass forming ability, all the four compositions have almost the similar values and this indicates that

the glass forming ability of all the four compositions is the same. However from ΔT calculations, $\text{Co}_{57.6}\text{Fe}_{14.4}\text{B}_{19.2}\text{Si}_{4.8}\text{Cr}_4$ was found to be the best glass former amongst the four alloys. Therefore, we conclude that there is no correlation for ΔT parameter and reduced glass transition parameter for the $[\{\text{Co}_{(1-x)}\text{Fe}_{(x)}\}(0.75)\text{B}(0.2)\text{Si}(0.05)]_{96}\text{Cr}_4$ system.

CHAPTER 4

MAGNETIC PROPERTIES OF COBALT AND IRON BASED METALLIC GLASSES

4.1 Saturation Magnetization

The base composition of the alloy system that is being studied is $[\{Co_{(1-x)}Fe_{(x)}\}(0.75)B(0.2)Si(0.05)]_9Cr_4$. As the system comprises of two ferromagnetic elements (iron and cobalt), study of magnetic properties of this system is of special interest. The four alloys whose magnetic properties are being evaluated are $Co_{72}B_{19.2}Si_{4.8}Cr_4$, $Co_{64.8}Fe_{7.2}B_{19.2}Si_{4.8}Cr_4$, $Co_{57.6}Fe_{14.4}B_{19.2}Si_{4.8}Cr_4$ and $Co_{50.4}Fe_{21.6}B_{19.2}Si_{4.8}Cr_4$ which are fabricated by systematically substituting Co with increments of 7.2 at% Fe. Applying a maximum field of 200000 A/m, hysteresis loops for the four alloy compositions have been generated and is consolidated in figure4.1.

From the experimentally obtained data, we clearly notice a trend with substitution of cobalt with iron. As there is an increment in the percentage of iron in the alloy composition, from the hysteresis loops the saturation magnetization values for each of the alloys is changing. The substitution of 7.2 at% cobalt with iron in each of the alloys has an effect on the saturation magnetization of the composition. As iron which is known to have the highest magnetic moment among the existing available ferromagnetic elements, we can expect an orderly increase in the saturation magnetization value with 7.2 at% addition of iron to each alloy. From the M vs H plots, $Co_{72}B_{19.2}Si_{4.8}Cr_4$, which has no iron content has the lowest saturation magnetization value of 72.53 emu/g and with the substitution of 7.2 at% cobalt with iron, the saturation magnetization value of $Co_{64.8}Fe_{7.2}B_{19.2}Si_{4.8}Cr_4$ has increased to 91.93 emu/g.

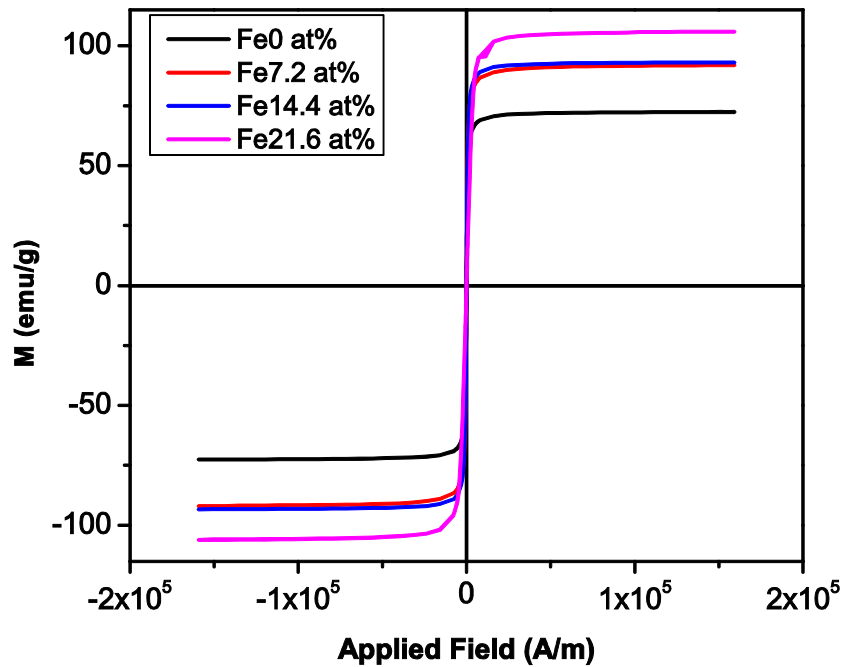


Figure 4.1 Consolidated M vs H curves for the amorphous melt spun Co-Fe ribbons.

Table 4.1 Corresponding saturation magnetization values for the compositions $\text{Co}_{72}\text{B}_{19.2}\text{Si}_{4.8}\text{Cr}_4$, $\text{Co}_{64.8}\text{Fe}_{7.2}\text{B}_{19.2}\text{Si}_{4.8}\text{Cr}_4$, $\text{Co}_{57.6}\text{Fe}_{14.4}\text{B}_{19.2}\text{Si}_{4.8}\text{Cr}_4$ and $\text{Co}_{50.4}\text{Fe}_{21.6}\text{B}_{19.2}\text{Si}_{4.8}\text{Cr}_4$.

Composition	Saturation Magnetization (emu/g)
$\text{Co}_{72}\text{B}_{19.2}\text{Si}_{4.8}\text{Cr}_4$	72.53
$\text{Co}_{64.8}\text{Fe}_{7.2}\text{B}_{19.2}\text{Si}_{4.8}\text{Cr}_4$	91.93
$\text{Co}_{57.6}\text{Fe}_{14.4}\text{B}_{19.2}\text{Si}_{4.8}\text{Cr}_4$	93.38
$\text{Co}_{50.4}\text{Fe}_{21.6}\text{B}_{19.2}\text{Si}_{4.8}\text{Cr}_4$	106.1

For the alloy comprising of 21.6 at% of iron the observed value of saturation magnetization is 106.1 emu/g which is much more higher. As it has been mentioned earlier, the magnetic moment of cobalt is less than iron and so, the replacement of cobalt with iron is enhancing the magnetic properties of these amorphous alloy compositions. In short, it can be summarized that with the addition of ferromagnetic elements, the saturation magnetization of system is improving.

However, the amorphous composition $\text{Co}_{57.6}\text{Fe}_{14.4}\text{B}_{19.2}\text{Si}_{4.8}\text{Cr}_4$ containing 14.4 at% of iron has a

saturation magnetization value of 93.38 emu/g which is almost equivalent to that of the composition $\text{Co}_{64.8}\text{Fe}_{7.2}\text{B}_{19.2}\text{Si}_{4.8}\text{Cr}_4$ which contains only 7.2 at% iron. This particular alloy composition which comprises of 14.4 at% iron fails to follow the trend shown by the three other compositions.

In order to explain the magnetic behavior of $\text{Co}_{57.6}\text{Fe}_{14.4}\text{B}_{19.2}\text{Si}_{4.8}\text{Cr}_4$ alloy, we try to relate few concepts of “*local-environment model*” where the sub-lattice magnetic moment changes were observed in DO_3 ordered structure (Fe_3Si) with varying concentrations of impurity.

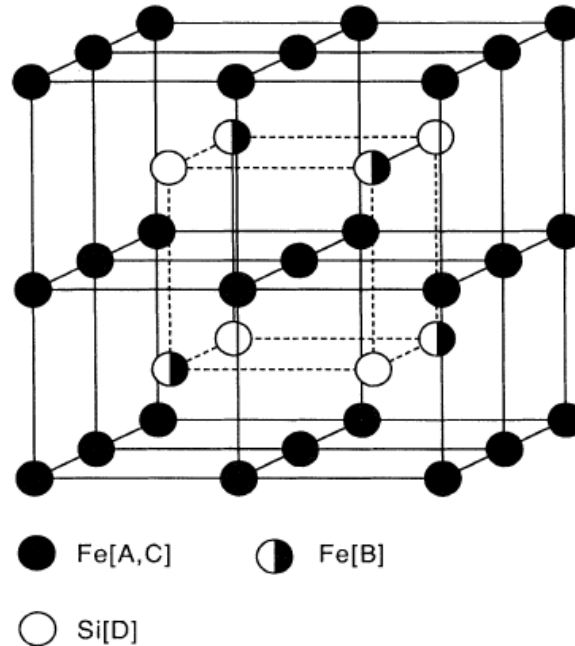


Figure 4.2 Schematic of DO_3 structure of Fe_3Si crystal. [59]

Figure 4.2 is a crystal structure which is similar to fcc bravais lattice comprising of four fcc sub-lattice of Fe_3Si crystal. Saturation magnetization measurements have led to a conclusion that the magnetic moment of Fe sitting on A and C sites is less than the Fe atom on B site. This is because Fe atoms on A and C sites have four Fe[B] and four Si[D] as their nearest neighbors with tetrahedral symmetry whereas Fe atoms on B site are surrounded by eight Fe [A,C] nearest

neighbors similar to that of BCC iron. Thus, the local magnetic interaction between the elements result in a change in the overall magnetic moment [59].

Furthermore, the effect of composition change on magnetic moments has also been discussed considering the alloy $\text{Fe}_{3+y}\text{Si}_{1-y}$ which has a disordered DO_3 structure where $0.4 \leq y \leq 1.0$. The magnetic properties of this alloy change significantly with variation in number of neighboring Fe atoms. As the percentage of iron is increased, Fe atoms prefer to occupy the D sites (Si sites). Thus the magnetic moment of the A and C site increases with increasing number of Fe atoms as the negative moment of Si is being replaced by significantly large positive value. Having an increased number of ferromagnetic atoms in the neighborhood, the overall magnetic moment is subjected to change.

We now try to apply the same theory to our amorphous ribbons whose magnetic properties show a significant change with varying the composition.

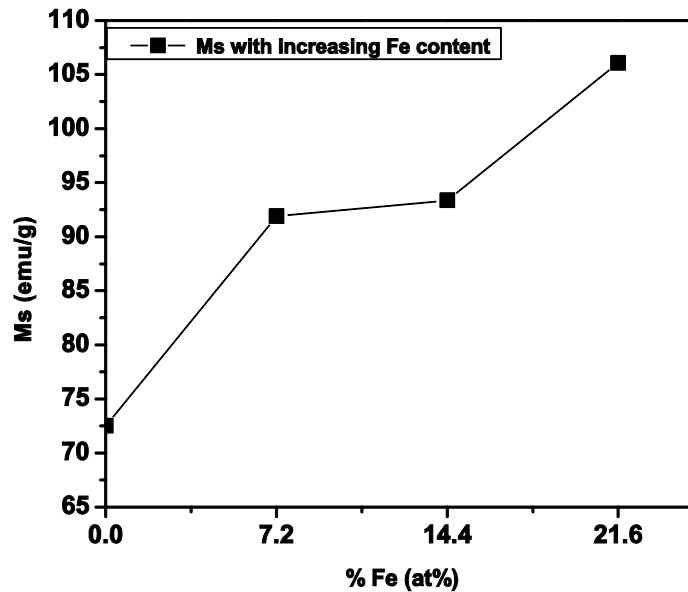


Figure 4.3 Graphical representation of increase in saturation magnetization with increasing iron concentration in the composition.

As discussed above, the addition 14.4 at% of iron has no significant difference in its magnetic properties in comparison to the alloy with 7.2 at% iron but the rest of the alloys surely show a remarkable difference. Being the best glass former among the four alloys with highest ΔT , we expect $\text{Co}_{57.6}\text{Fe}_{14.4}\text{B}_{19.2}\text{Si}_{4.8}\text{Cr}_4$ to have a very compact randomly packed dense structure.

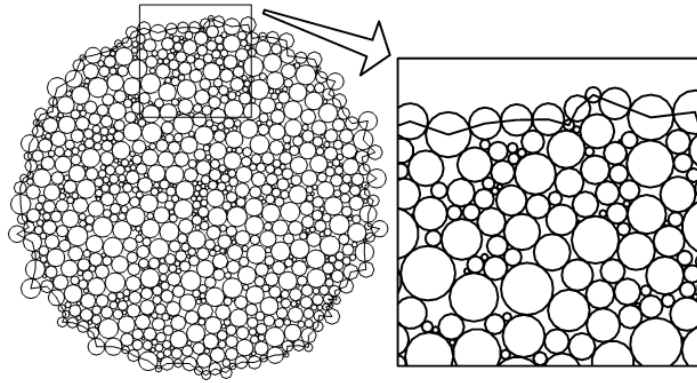


Figure 4.4 Schematic:metal (big circles) and metalloid (small circles) random dense packing [61].

BMGs are known for their unique feature of non-crystallinity. So, there are no grain boundaries for the amorphous materials and the atomic arrangement in these materials not periodic as in crystalline materials and hence this type of arrangement is called a random packing. Higher the GFA of a BMG, the more compact and dense is the packing of the atoms. As ΔT is one of the most commonly used parameters to measure the GFA, the alloy $\text{Co}_{57.6}\text{Fe}_{14.4}\text{B}_{19.2}\text{Si}_{4.8}\text{Cr}_4$ will have an atomic arrangement that is rigidly packed. To obtain such a structure, the interaction between the metal and the metalloid atoms should be high. For this to take place, the smaller radii atoms which are essentially metalloids fill up the voids that are formed by any of the large radii atoms interaction. Since the ferromagnetic transition metals in our composition are larger in diameter than the metalloids, there will be an increase in the magnetic and non-magnetic interaction. In other words, the ferromagnetic atom is expected to have more number of metalloids neighbors. This magnetic – nonmagnetic interaction will reduce

the local magnetic moment in the sample which plays a key role in the overall compositional magnetic moment. Although there has been an increase of 7.2 at% of ferromagnetic substance – iron, due to its dense random atomic packing there is no significant increase in the overall magnetic moment of $\text{Co}_{57.6}\text{Fe}_{14.4}\text{B}_{19.2}\text{Si}_{4.8}\text{Cr}_4$ from $\text{Co}_{57.6}\text{Fe}_{7.2}\text{B}_{19.2}\text{Si}_{4.8}\text{Cr}_4$.

4.2 Coercivity

Unlike the crystalline materials, amorphous alloys are free from grain boundaries and dislocations which act as major pinning site that restrict the domain wall motion. However, though the major obstacles to domain motion are absent, there are other defect structures that affect the coercivity from being negligible. In the past few years, few methods have been brought forward to study these defect structures with the consideration that despite of their chemical inhomogeneity and random anisotropy, the ground states magnetic spins are aligned as parallel as the spins in ferromagnetic alloy. Elastic stresses also called as quasi-dislocation dipoles, fluctuations in local anisotropy and structural relaxation, all of these contribute to the pinning of domain wall motion. To quantify the coercivity of these amorphous alloys, we need to understand the possible pinning sites for domain wall motion. Spin – orbit coupling energy, local magnetization, unique axis of anisotropy and spin quantum number contribute to non-uniform spontaneous magnetization alignment. Thus, each magnetic ion acts as an inhomogeneity which provides a pinning site for domain wall motion restriction [60].

The following equation corresponds to the coercivity generated in the material due to domain walls.

$$H_c^i = \frac{1}{M_s} \frac{(\rho M)^{1/2}}{\sqrt{2F_B}} \frac{\langle \Omega \rangle}{\delta_0^{1/2}} \left[\frac{8}{5} ((K)^2 + \sigma_k) + \frac{11}{60} \frac{\sigma_c}{2\delta_0^4} \right]^{1/2} \times \left[\frac{\ln L_3}{2\delta_0} \right]^{1/2} \quad (1)$$

where, F_B = domain wall area, M_s = saturation magnetization of the alloy, ρ_m = magnetic ions density, σ_c = dispersion of exchange energy, σ_k = dispersion of anisotropy, L_3 = width of the

domain. The different factors contributing to this coercivity are the fluctuation energies that generate a wall energy that is dependent on, (a) the domain wall position, (b) pinning forces due to these energy fluctuations, (c) position of the pinning forces, (d) dispersion anisotropy, and (e) exchange energy.

In most of the amorphous alloys, there is some short range ordering which forms a bernal structure with transition metal atoms and metalloids. Few atomic pairs within these structures will have their magnetic moments oriented parallel to spontaneous magnetization which leads to induced anisotropy. Material properties are subjected to increase in fluctuations with short range ordering. In the case of local anisotropy, fluctuations are caused in K and C by a factor of n_{cl} which denotes the number of atoms forming the cluster in short range ordering. Equation (2) corresponds to the coercivity contributing from short range ordering where the arrow brackets represent average of its corresponding enclosed values.

$$H_c^{so} = \frac{1}{M_s} \frac{(\rho M)^{1/2}}{\sqrt{2F_B}} \frac{n_{cl}^{1/2} \langle \Omega \rangle}{\delta_0^{1/2}} \times [\langle K \rangle^2 + \sigma_k]^{1/2} \left[\frac{\ln L_3}{2\delta_0} \right]^{1/2} \quad (2)$$

As per the above discussion, the inhomogeneties in the amorphous alloys are the pinning centers for domain wall motion which correspond to stress sources. Exerting varied stress fields, Quasidislocation dipoles are formed with the stacking of free volume during rapid quenching which become the main source of elastic stresses. With D corresponding to the width of the dipole, burgers vector denoted by b , ρ_{dip} giving the density of quasidislocation dipoles and ΔV denoting volume contraction due to quasidislocation dipole, the coercivity due to stress sources is given by

$$H_c^\sigma = \frac{12}{M_s} \frac{(\rho M)^{1/2}}{\sqrt{30F_B}} G \lambda_s b \times \frac{\Delta V}{\delta_0^{1/2}} \rho_{dip}^{1/2} \left[\frac{\ln L_3}{2\delta_0} \right]^{1/2} \quad (3)$$

Two other factors effecting the coercivity of a material are surface irregularities and magnetic after effects. Topology of the material is definitely influencing the coercivity. With change in the material thickness, the coercivity also varies and the method used to reduce the thickness also has its influence on coercivity. Similarly, upon annealing the material undergoes structural relaxation where the atoms with smaller radii or the free volume displacement try to rearrange. With these structural adjustments, the magnetic interaction between spontaneous magnetization and atom pair axes lead to a decrease in interaction energy which is energetically favorable.

All the five parameters discussed here have an influence on the materials coercivity which is estimated with the use of statistical potential theory. Neglecting the surface irregularity effects the overall coercive field is given by

$$H_c^{total} = \sqrt{(H_c^{\sigma})^2 + (H_c^i)^2 + (H_c^{so})^2} + H_c^{rel} \quad (4)$$

On the basis of the different factors discussed, we try to analyze the effect of iron addition on coercivity of the four amorphous alloys. The change in coercivity with a systematic increment of 7.2 at% iron in each alloy is graphically represented below.

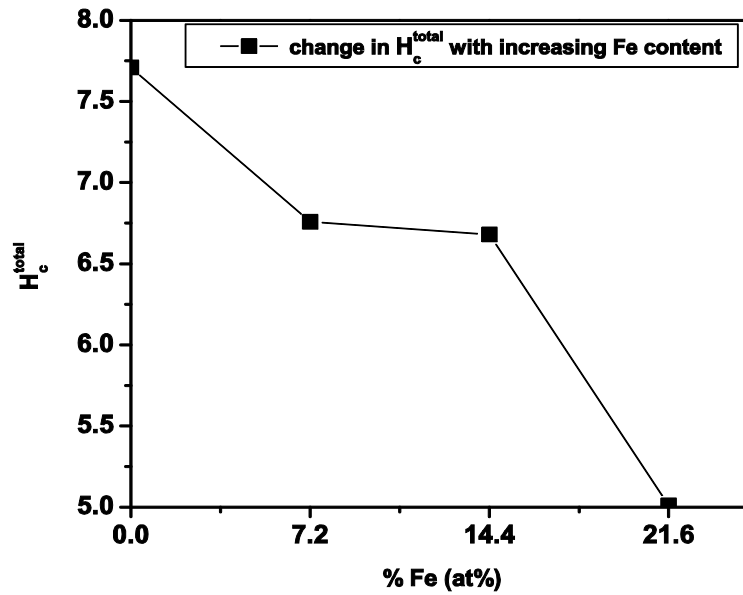


Figure 4.5 Graphical representation of effect of iron concentration on coercivity.

As it can be noticed, the composition which has no trace of iron, $\text{Co}_{72}\text{B}_{19.2}\text{Si}_{4.8}\text{Cr}_4$, has highest coercivity (7.71 A/m) amongst the four compositions and the alloy with 21.6 at% of iron, $\text{Co}_{50.4}\text{Fe}_{21.6}\text{Si}_{4.8}\text{Cr}_4$, has the lowest (5.01 A/m). This decrease in coercivity with the replacement of cobalt with iron can be explained in terms of intrinsic inhomogeneties. As we know that each magnetic ion is a source of such inhomogeneties and is a potential site that behaves as a pinning center for domain wall motion. As cobalt of atomic radius 125 pm is being substituted with iron of radius 126 pm, the iron atom occupies more space than cobalt. So, the number of iron atoms per unit volume will be less than the number of cobalt atoms before being substituted. With this decrease in ferromagnetic atoms per unit volume, the magnetic ion concentration in a domain wall also reduces. Thus, the magnetic ions which are potential sites as pinning center become less and favor domain wall motion. Thus the amount of restriction that a domain wall experiences is diminishing with increase in iron substitution for cobalt which results in lower coercivity.

Since the four compositions belong to the same system, assuming that the domain wall size, area, length remain constant can be of additional support to explain this trend. From equation (4),

$$H_c^{Total} \propto \frac{1}{M_s} \quad (5)$$

The product of the two parameters, H_c^{Total} and M_s for all the four compositions remains a constant with an acceptance of 10%. As we observe from the data, the saturation magnetization (M_s) of the composition is increasing with increase in the percentage of iron being substituted and the coercivity dropping. Thus the trend of coercivity falls in line with the relationship given by equation (5) and this behavior of alloys is justified.

4.3 Thermomagnetic Stability

After obtaining the room temperature magnetic properties of the four compositions $\text{Co}_{72}\text{B}_{19.2}\text{Si}_{4.8}\text{Cr}_4$, $\text{Co}_{64.8}\text{Fe}_{7.2}\text{B}_{19.2}\text{Si}_{4.8}\text{Cr}_4$, $\text{Co}_{57.6}\text{Fe}_{14.4}\text{B}_{19.2}\text{Si}_{4.8}\text{Cr}_4$, and $\text{Co}_{50.4}\text{Fe}_{21.6}\text{B}_{19.2}\text{Si}_{4.8}\text{Cr}_4$, the stability of these properties at high temperatures is of interest. To study the effect of temperature on the magnetic properties, the four alloys were heated up from room temperature to 850 K to measure their respective curie points (Figure 4.6a). A slight increase in temperature of a system has its effect on atomic vibrations. Therefore, taking the system to a temperature of 850 K induces very high thermal vibrations on an atomic scale. Since the atomic magnetic moments are free to rotate, increase in temperature results in randomization of the magnetic moments and thus misaligning the ordered magnetic domain. This misalignment of magnetic moments results in reduced magnetization. As the temperature is slowly raised from room temperature, thermal vibrations in the atomic scale also increase which directly affect the magnetic moment alignment.

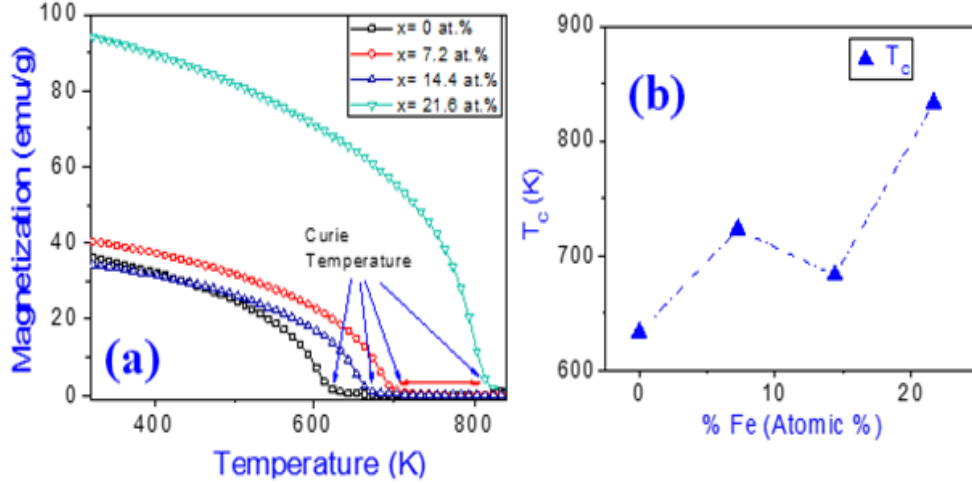


Figure 4.6 (a) Thermomagnetic curves for the four different alloy compositions and (b) Dependence of curie temperature on the percentage of iron content.

The alloy with highest iron content has the highest curie temperature (Figure 4.6b). When the temperature is normalized by the glass transition temperature of the respective alloy, curie temperatures for the compositions with 0, 7.2 and 14.4 at% Fe lie well below their glass transition temperature. However, for the alloy with 21.6 at% Fe, the curie point is well above the glass transition temperature. This could be due to the strong ferromagnetic ordering with increased iron concentration that is owing to synergistic *s-d* hybridization even at elevated temperatures.

4.4 Phases Formed after Crystallization

In order to compare the magnetic behavior of the amorphous and crystalline compositions, the fully amorphous metallic glass ribbons of the composition $\text{Co}_{72}\text{B}_{19.2}\text{Si}_{4.8}\text{Cr}_4$, $\text{Co}_{64.8}\text{Fe}_{7.2}\text{B}_{19.2}\text{Si}_{4.8}\text{Cr}_4$, $\text{Co}_{57.6}\text{Fe}_{14.4}\text{B}_{19.2}\text{Si}_{4.8}\text{Cr}_4$ and $\text{Co}_{50.4}\text{Fe}_{21.6}\text{B}_{19.2}\text{Si}_{4.8}\text{Cr}_4$, were heated up to 900 K. Since the crystallization events for all the four alloys occur way below 900 K, the amorphous morphology has completely transformed to crystalline. Figure 4.7 shows the SEM micrographs of the fully crystalline samples for the four compositions. The microstructures for the four compositions is similar to that of eutectic structure. All the four alloys have different

phases distinguishable by their color contrast (white, grey and black). In order to understand the magnetic properties of these crystalline samples, these phases are to be identified and evaluation of properties of these phases can be correlated to their magnetic nature. Also, assuming that the size of the grains is equal to that of the phases, it is evident from the micrographs that the grains are of submicron size. Therefore, the effect of grain size is directly observed with the change in coercivity of these crystalline samples.

Experimentally obtained hysteresis curves for the crystalline samples are represented in the figure 4.8. While our main goal is to compare the magnetic properties of amorphous and the crystalline alloys each of the magnetic properties are carefully evaluated. As we expect, due to the grain size, the coercivity of the crystalline samples is much higher compared to that of amorphous. There is a prominent increase in the hysteresis area for all the four compositions. Therefore, the obtained coercivity values for the fully crystalline alloys with 0, 7.2, 14.4, and 21.6 at% of iron are 16.5k, 12.2k, 7k, and 7.1k A/m respectively which categorize these alloys as semi hard magnetic materials. Another compelling observation is that, the coercivity values show a decreasing trend with an increase in iron concentration. The composition with no iron content has a coercive field of 16.5k A/m which is twice that of the composition bearing 14.4 at% and 21.6 at% of iron. Since coercivity is a parameter with structural dependency, it is correlated to grain size based on two hypothesizes. First, when the grain size is considered to be larger than the magnetic exchange length.

$$H_c = 3 \sqrt{\frac{kT_c k_1}{\alpha M_s}} \frac{1}{D} \quad (6)$$

where D is the size of the crystallite, T_c is the curie temperature, K_I is magneto-crystalline anisotropy and M_s is saturation magnetization. The magnetic exchange length is given by

$$L = \sqrt{\frac{A}{k_1}}, A \text{ is the exchange stiffness constant.}$$

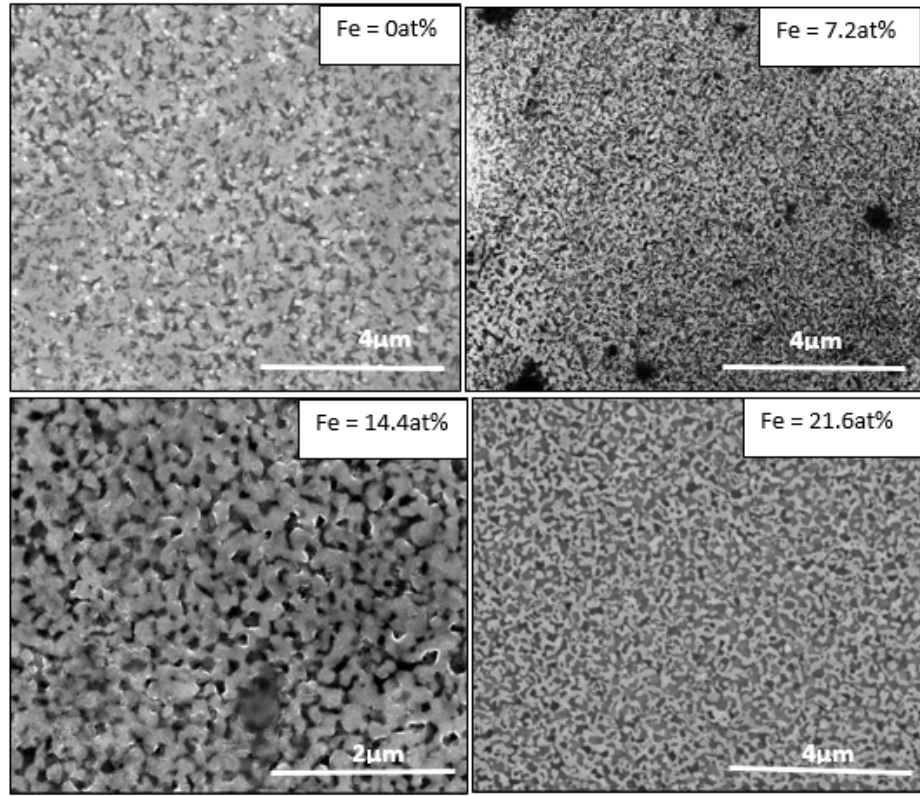


Figure 4.7 SEM micrographs of fully crystallized Co₇₂B_{19.2}Si_{4.8}Cr₄, Co_{64.8}Fe_{7.2}B_{19.2}Si_{4.8}Cr₄, Co_{57.6}Fe_{14.4}B_{19.2}Si_{4.8}Cr₄, and Co_{50.4}Fe_{21.6}B_{19.2}Si_{4.8}Cr₄ alloys with each image marked by its atomic percentage of iron concentration.

The second hypothesis is when the grain size is smaller than magnetic exchange length. The coercivity is proportional to the size of the crystallite. Then the following equation is satisfied with each grain behaving as a single domain.

$$H_c = \frac{P_c k_1^4 D^6}{\mu_0 M_s A^3} \quad (7)$$

P_c = constant of the order of unity and μ_0 is permeability of free space.

Increasing the grain size (assuming grain size to be equal to phase), is affecting the coercivity values. Due to increasing iron concentration there is a significant drop in coercivity values which can be attributed to increase in size of the crystallites. The first hypothesis in which

the coercivity is inversely related to crystallite size falls in line with the observations. Therefore, it can be concluded that though grains are about submicron in size, they are larger than the magnetic exchange length.

Not just the coercivity values, but the saturation magnetization of the crystalline samples is also found to be higher than the amorphous alloys. The experimentally obtained M vs H curves for the crystalline compositions is represented in the figure 4.8. A trend similar to that of the amorphous materials is followed in the crystalline samples as well. With increasing ferromagnetic iron concentration, the saturation magnetization value is further enhanced. The saturation magnetization values for the composition with 0, 7.2, 14.4, and 21.6 at% iron content are 80.6 emu/g, 104.9 emu/g, 147.2 emu/g, and 152.3 emu/g respectively. Comparing these values to those of amorphous alloys shows that the crystalline materials have superior magnetic properties. However, this can be achieved only with a compromise on coercivity. With such high values of coercive field, crystalline samples are no longer falling under the category of soft magnets. In order to better understand the superior magnetic properties of these crystalline samples, phase analysis was done.

Various ferromagnetic phases that formed upon crystallization explain the significant increase in saturation magnetization values. XRD patterns for the compositions containing 0 at% and 7.2 at% iron have similar peak positions. These crystalline peaks correspond to cobalt rich phases (Co_2B , Co_3B , and Co_2Si). While the compositions with 14.4 at% and 21.6 at% iron have similar XRD pattern with their peak positions corresponding to cobalt and iron rich phases ($(\text{Co}, \text{Fe})_2\text{B}$, Co_3B , and Co_2B). Co_2B and Fe_2B are strong ferromagnetic phases which show spontaneous magnetization.

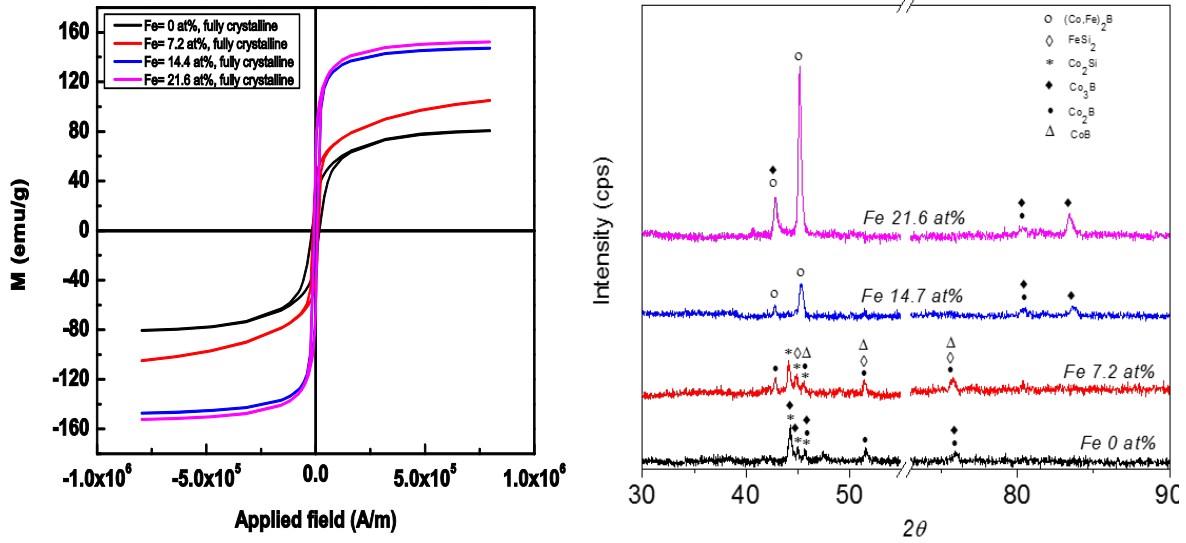


Figure 4.8 M vs H hysteresis curves for fully crystalline samples and their respective XRD patterns.

Table 4.2 Summarized saturation magnetization values and their corresponding phases affecting these values for fully crystalline samples.

Composition	Saturation magnetization in amorphous state (emu/g)	Saturation magnetization in crystalline state (emu/g)	Phases affecting this change
$\text{Co}_{72}\text{B}_{19.2}\text{Si}_{4.8}\text{Cr}_4$	72.53	80.60	Co_2B , Co_3B , and Co_2Si
$\text{Co}_{64.8}\text{Fe}_{7.2}\text{B}_{19.2}\text{Si}_{4.8}\text{Cr}_4$	91.93	104.9	Co_2B , Co_3B , and Co_2Si
$\text{Co}_{57.6}\text{Fe}_{14.4}\text{B}_{19.2}\text{Si}_{4.8}\text{Cr}_4$	93.38	147.2	$(\text{Co}, \text{Fe})_2\text{B}$, Co_3B , and Co_2B
$\text{Co}_{50.4}\text{Fe}_{21.6}\text{B}_{19.2}\text{Si}_{4.8}\text{Cr}_4$	106.1	152.3	$(\text{Co}, \text{Fe})_2\text{B}$, Co_3B , and Co_2B

It is evident from Table 4.1 that the percentage increase in saturation magnetization for compositions $\text{Co}_{57.6}\text{Fe}_{14.4}\text{B}_{19.2}\text{Si}_{4.8}\text{Cr}_4$ and $\text{Co}_{50.4}\text{Fe}_{21.6}\text{B}_{19.2}\text{Si}_{4.8}\text{Cr}_4$ is much higher than that of the other two. This can be attributed to the presence of Fe_2B peak visible in the XRD pattern (figure 4.8). Through computational methods and experiments [61], it has been found that the atom averaged magnetic moment of Fe_2B is higher than Co_2B . Therefore the significant increase

in saturation magnetization values for the crystalline samples is due to the formation of these strong ferromagnetic phases and the exceptionally high saturation magnetization values for the compositions with 14.4 at % and 21.6 at% iron due to Fe_2B phase. The relative peak intensity corresponding to Fe_2B phase is higher than that of Co_2B phase.

4.5 Metastable Phases

The alloy with composition $\text{Co}_{72}\text{B}_{19.2}\text{Si}_{4.8}\text{Cr}_4$ has two prominent crystallization peaks while the other compositions have one sharp single crystallization peak. So, in order to study the magnetic properties of metastable crystalline phases, annealing experiments were done for each of the intermediate peak temperatures. Path 1, path 2, path 3 are the three heating paths that were chosen. Path 1 and path 2 were annealed for 0 minutes and 5 minutes at the two intermediate peak temperature while path 3 heats the sample to a temperature above the two crystallization peaks and back to room temperature. Path 1 and path 2 go to a maximum of 800K and 850K and annealed at these temperatures for 0 and 5 minutes respectively.

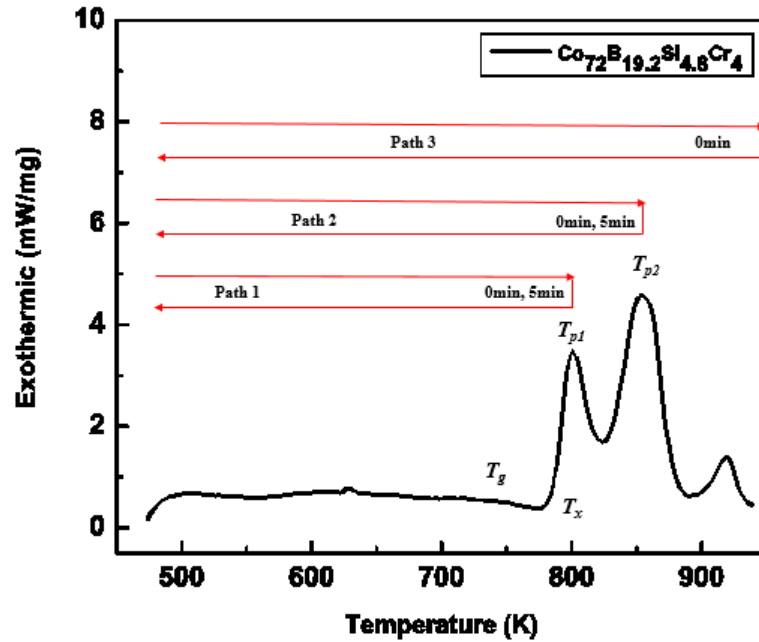


Figure 4.9 DSC plot for the composition $\text{Co}_{72}\text{B}_{19.2}\text{Si}_{4.8}\text{Cr}_4$ with T_g , T_x , T_{p1} , and T_{p2} denoting the glass transition, crystallization and the two intermediate peak temperatures.

Heating to 973K and cooling down to room temperature is path 3 which forms a completely crystalline structure whose magnetic properties have been discussed in section 4.3. With the help of M vs H curve measurements and XRD patterns, the properties of metastable crystalline phases occurring from path 1 and path 2 have been evaluated. The following figure 4.10 shows the variation of magnetic properties with different heat treatment cycles. In order to better understand their magnetic behavior, their corresponding XRD patterns have been evaluated.

Annealing treatment at the temperature 800K for 5 minutes has yielded better magnetic properties when compared to rest of the heat treatments. The amorphous alloy shows the least saturation magnetization values while the annealed samples show about 10-15 units of increment in the saturation magnetization values and the annealing treatments make the coercivity higher which is deteriorating the soft magnetic property shown by the amorphous alloy.

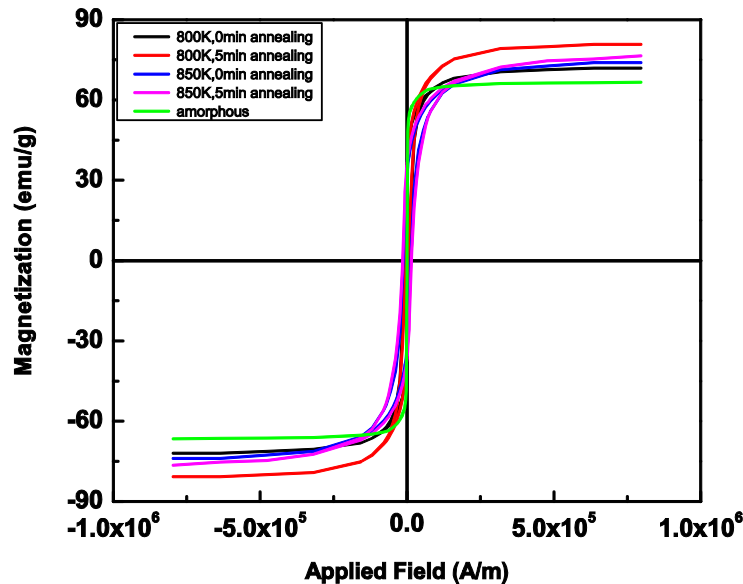


Figure 4.10 M vs H hysteresis curves for the composition $\text{Co}_{72}\text{B}_{19.2}\text{Si}_{4.8}\text{Cr}_4$ after annealing at 527°C and 577°C for 0 and 5 minutes.

However, the coercivity values obtained by heat treatment at 800K for 0 minutes and 5 minutes are 5.7k A/m and 5.9k A/m which is very close to the maximum limit that categorizes soft magnetic materials. Since the values are just slightly higher than the boundary limit, a few changes in the annealing treatments can adjust the coercivity in such a way that it falls under soft magnetic category. The saturation magnetization obtained by path 1 annealing treatment is similar to that obtained by path 3 (fully crystallized). Table 4.1 summarizes the magnetic properties of the five different alloys including the fully crystallized samples. The coercivity of the sample annealed at 800K for 5 minutes is three times less than that of the fully crystallized sample. Thus, the path 1 annealing for 5 minutes can be considered as the best heat treatment amongst the four annealing conditions to enhance the magnetic properties.

To identify the evolved ferromagnetic phases that are responsible for the increase in saturation magnetization and coercivity, phase analysis from XRD patterns was done for samples annealed at 800K and 850K for 5 minutes.

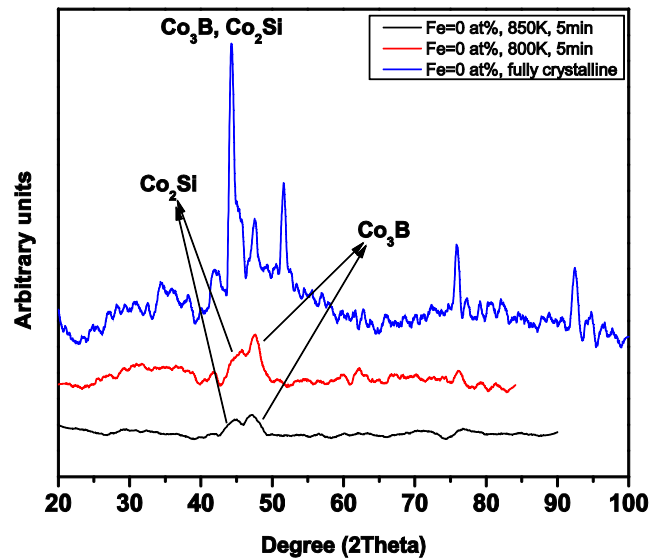


Figure 4.11 XRD pattern for the composition $\text{Co}_{72}\text{B}_{19.2}\text{Si}_{4.8}\text{Cr}_4$ showing the evolution of nano sized ferromagnetic phases when annealed at 800K and 850K for 5 minutes.

Broadening of the peaks at 44° and 47° for the annealed samples clearly indicate the possibility of evolution of nano crystallites. With reference to Y. Liu et al. [62] and G.F. Zhou et al. [63], the broad peak forming at about 44° corresponds to Co_2Si nano crystallites and the one at approximately 47° corresponds to Co_3B . These three nano crystalline phases that are ferromagnetic which could be the cause for the enhancement of magnetic properties. The superior magnetic properties attained via path 1 annealing treatment for 5 minutes can be attributed to Co_3B formation. The broad peak corresponding to Co_3B is much more prominent than the other phases and also has better magnetic moment compared to the other phases which explains the superior magnetic behavior.

From the XRD peaks, we have concluded that the broadening of peaks for annealed samples is attributed to the formation of nano crystalline phases. Thus, in comparison, the size of the crystal is bigger for fully crystalline samples than the annealed. Since the coercivity is dependent on material structure, the size difference in the crystallites is effecting the coercive field. As, the annealing treatments are forming nano crystallite phases, the coercivity values are way too smaller than the fully crystalline material. Therefore, from the summarized table 4.1, we notice that coercivity is directly related to the crystallite size. Thus equation (7) satisfies this present trend and so, we can conclude that the grain size of these ferromagnetic phases is larger than the magnetic exchange length.

Table 4.3 Summarized magnetic properties of $\text{Co}_{72}\text{B}_{19.2}\text{Si}_{4.8}\text{Cr}_4$ after annealing at different conditions.

Annealing condition		M_s (emu/g)	Coercivity (A/m)
Amorphous		66.7	7.7
800K	0 min	71.9	5.7k
	5 min	80.8	5.9k
850K	0 min	74	12.7k
		76.5	14.8k
Fully crystalline		80.6	16k

CHAPTER 5

MECHANICAL AND WEAR BEHAVIOR OF COBALT AND IRON BASED METALLIC GLASSES

5.1 High Energy Mechanical Milling

In order to mechanically activate the surface, high power ball milling technique was used on iron based metallic glass particles. The composition of the amorphous powder particles is $\text{Fe}_{48}\text{Cr}_{15}\text{Mo}_{14}\text{Y}_2\text{C}_{15}\text{B}_6$. The size of the particles vary from 10-40 μm . A lot of research has been done on the effect of ball milling on structural changes of amorphous alloys. Nano crystalline solids have unique physical and chemical properties and it is also believed that the catalytic response of nano size crystals is higher when compared to that of crystalline materials. These nano sized crystallites can be fabricated by three basic mechanisms and they are evaporation by condensation process in inert atmosphere, heat treatment at temperatures below crystallization, and mechanical deformation. With the application of mechanical forces, it is possible to generate very fine scale stable and metastable crystalline phases [64]. Similar concept is being extended to this particular composition. Detailed analysis on structure morphological changes that occur on the spherical iron based amorphous particles by varying the ball milling time has been done. The surface of iron based metallic glass micro-particles were activated using high speed mechanical milling in a liquid medium (methanol). The as received amorphous powder was placed in a high purity Zirconia jar with different diameter balls made up of high-alumina. The rotation speed during milling were kept at 500 rpm and the time selected for milling was 9 hr and 12 hr. Figure 5.2 illustrates the morphology of the as received amorphous particles, which are spherical, extraordinarily smooth surface with particle size within the range of 10-40 μm .

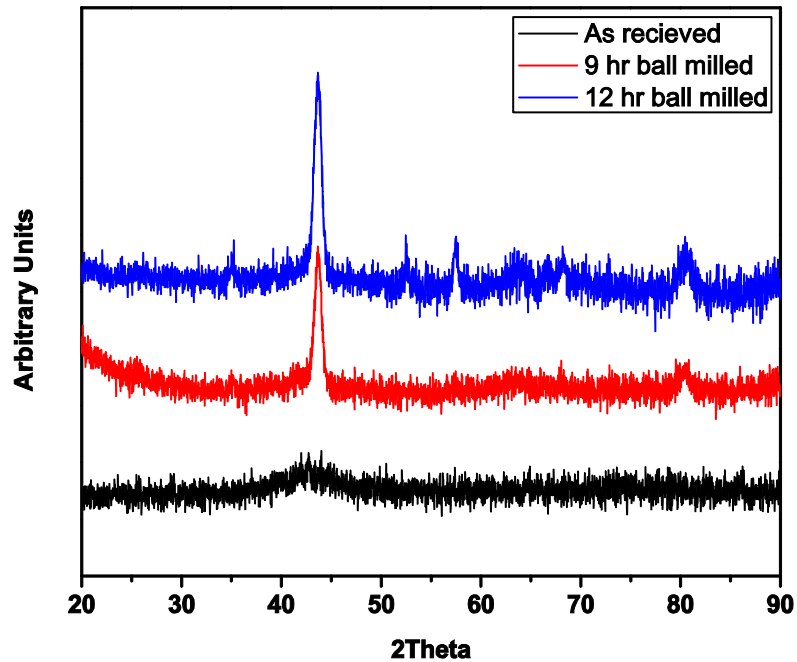


Figure 5.1 XRD pattern for the as received amorphous, 9 hr ball milled, and 12 hr ball milled iron based metallic glass powder.

XRD (Figure 5.2) of as-received amorphous particles (i.e. 0 hr milled) shows a broad area hump depicting the fully amorphous nature of the particles. After mechanical milling of 9 hours, there has been no substantial amount of crystallization observed in the XRD. However, by increasing milling time to 12 hours a wide range of crystalline peaks appeared in the XRD. Correlating the full width half maxima (FWHM) of the peaks by Debye-Scherrer equation we can expect the formation of nanocrystals. Nevertheless, to confirm this SEM and TEM imaging was done for the 9 hour ball milled particles. From the images, it is evident that the particles are no more spherical.

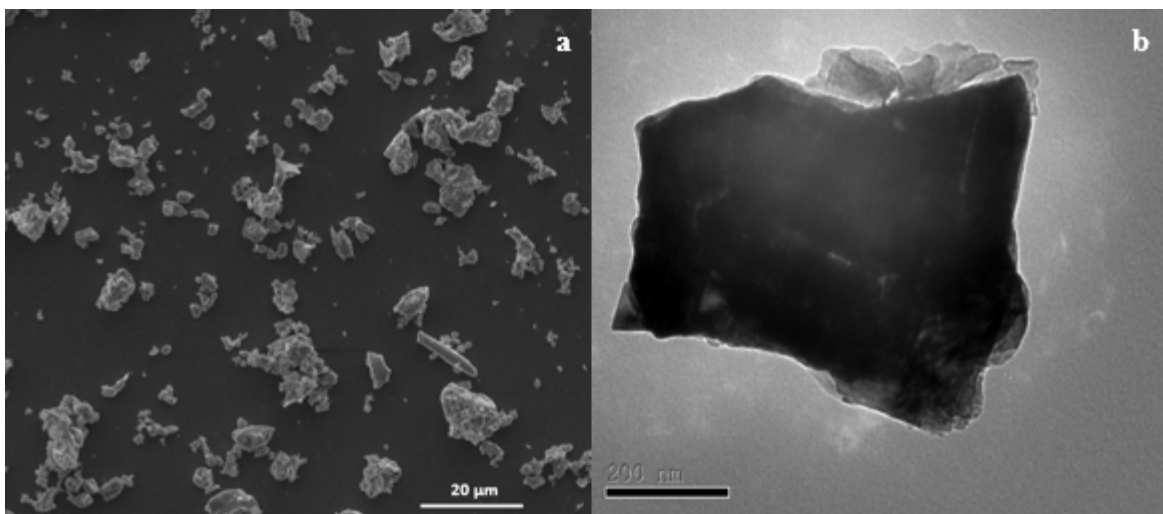


Figure 5.2 (a) SEM image and (b) TEM image of 9 hour ball milled iron based metallic glass of composition $\text{Fe}_{48}\text{Cr}_{15}\text{Mo}_{14}\text{Y}_2\text{C}_{15}\text{B}_6$.

The spherical micro sized particles have broken down to flaky nano sized particles. With high speed mechanical milling, the reduction in particle size to such a small scale helps in increasing the activity of surface. The flaky nano particles thus formed have highly activate surface compared to the as received spherical particles.

5.2 Iron Based Metallic Glass Coating on Aluminum Substrate

So far, a wide variety of coatings and coating techniques have been used on Aluminum substrate in order to enhance its tribological properties. In the present study, we use microwave processing techniques to form a coating using an iron based BMG precursor on aluminum substrate that can significantly improve the mechanical properties. Microwave is an electromagnetic wave with wavelengths ranging from 1mm to 1m that correspond to frequencies 300MHz to 300GHz. Heating of a specimen by a conventional process transports thermal energy in the material by conduction which induces thermal gradients that cause non uniform heating. Thus a slow heating rate results in increasing the processing time. However, microwave processing is a unique method where a uniform volumetric heating is achieved. The principle involved in attaining this uniform heating is conversion of electromagnetic energy to thermal

energy that occurs at molecular scale. Dielectric properties of the material determine the influence of electromagnetic field. Thus when the microwaves come in contact with the dielectric material, rotation of dipoles and translation motion of free and bound charge takes place. Resistance to induced motion due to inertia, elastic and frictional forces cause the uniform heating of bulk material. As the microwaves approach the material, it prefers to couple with higher loss tangent material and thus help in selective heating of materials. Although microwave processing is advantageous compared to conventional heating, there are a few concerns that need to be addressed. Since the energy is transferred through electromagnetic field, any fluctuations in this field can result in a non-uniform heating rate. Also, since there are temperature effects on materials properties, any physical or compositional transformations attributing to change in dielectric properties will also lead to non-uniform heating. Therefore, understanding propagation and interaction of microwaves with the material is essential [65, 66].

In the present study, we utilized microwave processing to synthesize composite coatings from an iron based metallic glass powder with the nominal composition $\text{Fe}_{48}\text{Mo}_{14}\text{Cr}_{15}\text{Y}_2\text{C}_{15}\text{B}_6$. Pure aluminum was used as a substrate material. Figure 5.1a shows SEM image of the iron based amorphous powder that was used to develop coating. These particles have been mechanically sieved and narrowed down to a size limit. The Phase transformations that can occur in the amorphous structure as a function of temperature are indicated by glass transition and crystallization temperatures. There are two crystallization events for the amorphous composition $\text{Fe}_{48}\text{Mo}_{14}\text{Cr}_{15}\text{Y}_2\text{C}_{15}\text{B}_6$. The DSC plot for the amorphous Fe BMG is shown in Figure 5.1b with the first crystallization event occurring at 653°C , the other indicated at 684°C and the glass transition temperature is 575°C .

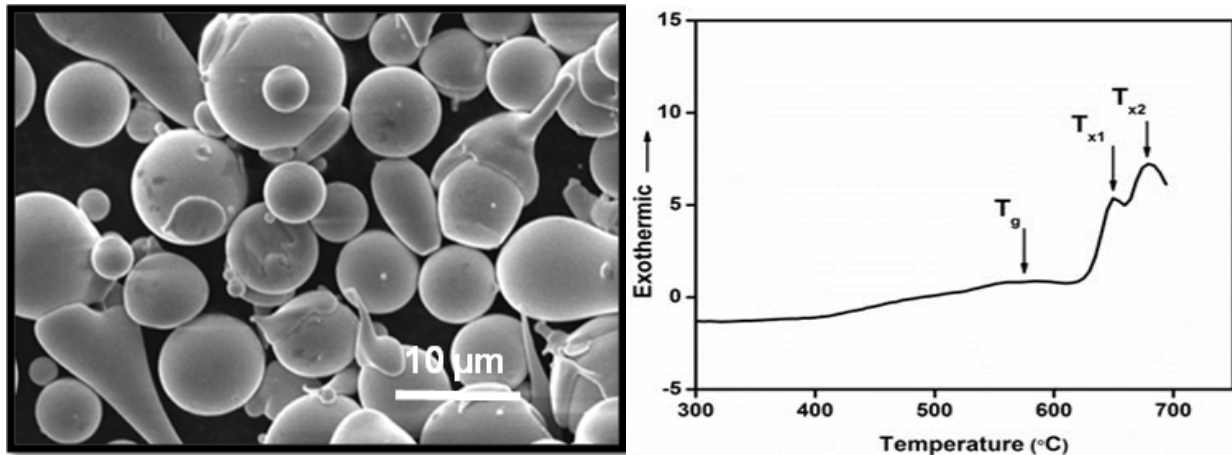


Figure 5.3 (a) SEM image of iron based metallic glass Fe₄₈Mo₁₄Cr₁₅Y₂C₁₅B₆ particles, (b) DSC plot for the composition Fe₄₈Mo₁₄Cr₁₅Y₂C₁₅B₆ showing the glass transition and crystallization events.

The amorphous Fe BMG powder that has been fabricated by gas atomization is evenly spread with a thickness of 1mm on the aluminum substrate. Activated carbon which is known for its high dielectric constant and dielectric loss factor is placed on the top of the coating. The substrate with metallic glass powder is placed in a graphite crucible and then covered by a susceptor material that has high absorbtivity for microwave radiation. The entire set up in the graphite crucible is placed in a microwave cavity which is exposed to microwaves of 2.54 GHz frequency and operating at 900 W power for a period of 6 minutes. This layer helps in enhancing the absorptivity of microwaves which gives a considerable increase in temperature. Exposure to microwave radiation of 2.54 GHz frequency forms a uniform defect free coating of on the aluminum substrate. A smooth metallurgical cladding interface is developed through microwave radiations. The average thickness of the coating on the aluminum substrate remained approximately 1 mm.

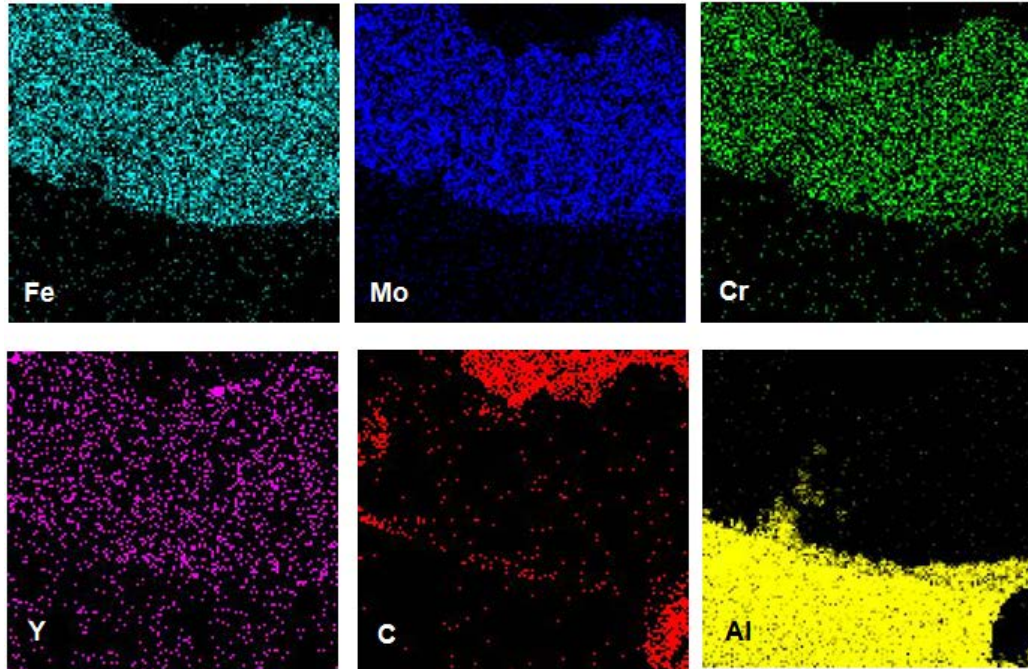


Figure 5.4 EDS elemental distribution of Fe, Mo, Cr, Y, C, and Al across the coating-substrate interface.

The EDS elemental mapping (Figure 5.2) at the coating-substrate interface depicts a strong bonding between the coating and substrate through elemental diffusion. Inter-diffusion of aluminum from the substrate to the coating and few of the coating elements such as iron, molybdenum and yttrium diffusing to the substrate can be clearly noticed (Figure 5.2). This inter-diffusion of elements at the coating-substrate interface is an indication of a strong bonding between the coating and substrate. Figure 5.3a shows the Fe BMG coating material, aluminum substrate, and the coating-substrate interface. There are three different phases indicated by three different color contrasts in the SEM image of the coating microstructure. Energy dispersive spectroscopic analysis of these phases gives an approximate elemental composition.

5.3 Wear Behavior of Metallic Glass Coating

As it has been noticed, there are three different phases formed in the coating. In order to study the characteristics of the coating, property evaluation of these three phases is necessary. Hardness and wear resistance are the two critical properties that need to be understood in order to evaluate the mechanical behavior of the coating. Load vs displacement curves obtained from nano-indentation on the coating revealed the presence of a softer phase and harder phase. The hardness and modulus of the iron rich phases denoted by B and C fall under the category of softer phase with similar hardness values. The obtained hardness of molybdenum rich phase is higher compared to B and C phases. Thus, the coating has a composite microstructure with the harder phases reinforcements distributed in the soft matrix yielding high strength. The hardness of B and C phases was found to be about 15 GPa which is harder than thermally sprayed $\text{Fe}_{48}\text{Mo}_{14}\text{Cr}_{15}\text{Y}_2\text{C}_{15}\text{B}_6$ coating and WC-Co coating. A scratch test was performed across the substrate and the coating. The profiler images obtained at the substrate and the coating give the wear volume loss. It was found that the composite coating has lower material loss compared to the substrate. The calculated material loss in the composite coating is about $1.57 \times 10^{-3} \text{ mm}^3$ and the substrate is $3 \times 10^{-3} \text{ mm}^3$. Therefore the significant deformation in the substrate compared to the coating that is illustrated in figure 5.4 is justified. With the significant difference in the volume loss at the substrate and the coating, the coating shows better wear resistance than aluminum.

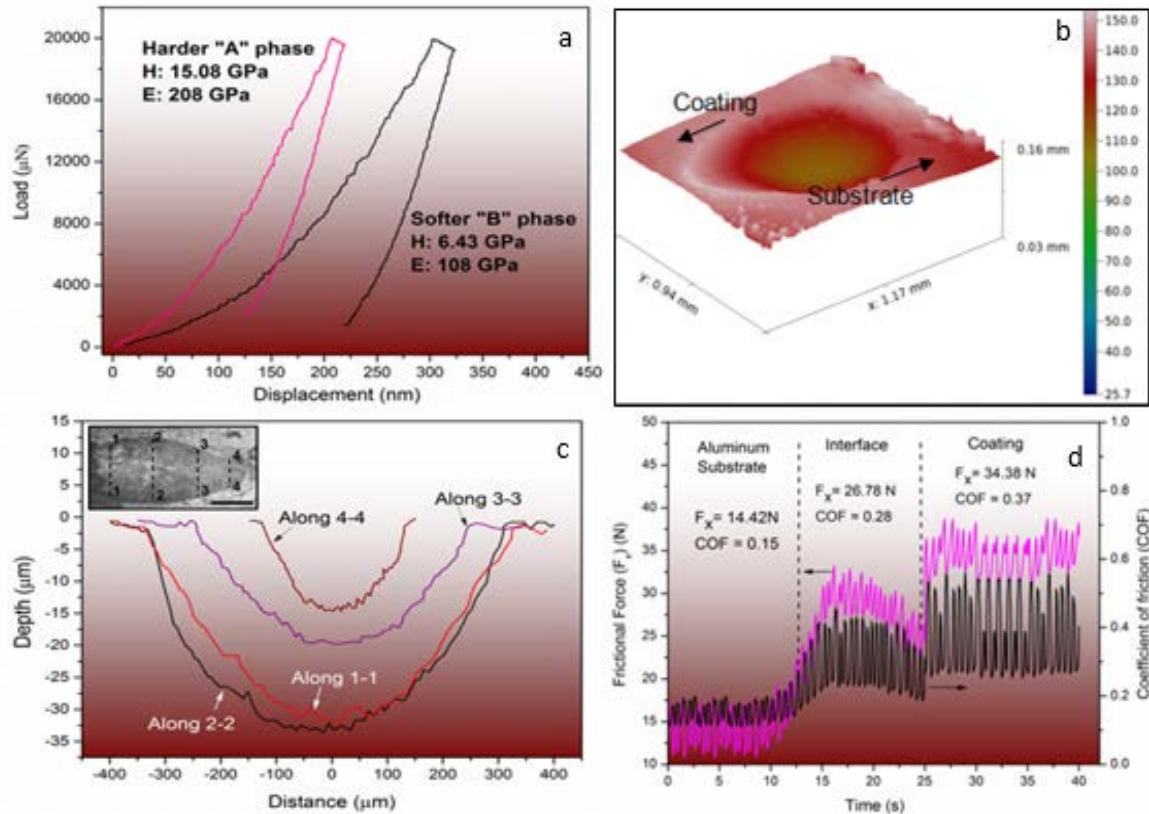


Figure 5.6 (a) Load vs Displacement curves for the hard and soft phase, (b) 3-D image of volume loss during scratch test, (c) & (d) Depth profiles and coefficient of friction for the substrate, interface and the coating.

Also, the depth profiles captured along the scratch show deeper indentations on the substrate which are approximately thrice as that of the coating and twice as that of the interface. This clearly indicates better hardness of coating than the substrate. The depth profile marked as 1-1 in the figure corresponds to the aluminum substrate while 4-4 corresponds to the composite coating. The depth profile represented by 3-3 is at the interface between coating and substrate. A measure of frictional force and coefficient of friction values significantly increase from the substrate to the coating. But such a high rise in coefficient of friction of coating contradicts its high hardness. Due to the abrasive action of wear, there is a possibility that harder phase reinforcement fracture that can cause an increase in coefficient of friction. Also, it has been reported earlier that a harder phase reinforcement in a composite causes an increment in

coefficient of friction [67]. Considering high frictional force and lower volume loss due to wear, it can be concluded that the coating is strongly adhesive with a good interfacial strength.

5.4 Hardness and Modulus by Nano-Indentation

Metallic glasses are known for exceptional high strength and hardness with great potential as structural materials. It has been observed that the shear modulus of metallic glasses is 10 – 30% less than crystalline materials where as its bulk modulus is nearly comparable. The nature of bonding and average electron density of metallic glasses and crystalline materials is comparable which explains their similarity in bulk modulus while the structural disorder causes softening that gives low resistance against shear. The inelastic rearrangement of atomic clusters occurs due to structural relaxation and is reversible upon unloading [68]. The heterogeneous deformation mechanism of bulk metallic glasses is the most intriguing area due to the absence of dislocations that are plastic flow promoters. They undergo localized shear band generation and the uninterrupted propagation of these shear bands leads to a catastrophic failure. A number of theories explaining the deformation mechanism have been proposed. The free volume model gives atomic scale mechanism responsible for failure of BMGs. The mechanism proposed in this model is similar to atomic diffusion. The atoms jump into the nearest free volume space creating the motion and the activation energy required for this movement is very low. Another predominant theory is shear band transformation. Local atomic rearrangements due to applied strain generates two types of thermally activated shear transformation. Argon [69] proposed that these transformation occur in the temperature range $0.6T_g - T_g$. In this temperature range, cluster of atoms try to rearrangement such that the applied strain is accommodated and this big cluster of atoms is also known as shear transformation zone (STZ). A continuous flow of shear strain is

generated when one STZ creates localized distortion further effects the surrounding and due to which larger shear transformation zones or shear bands are formed.

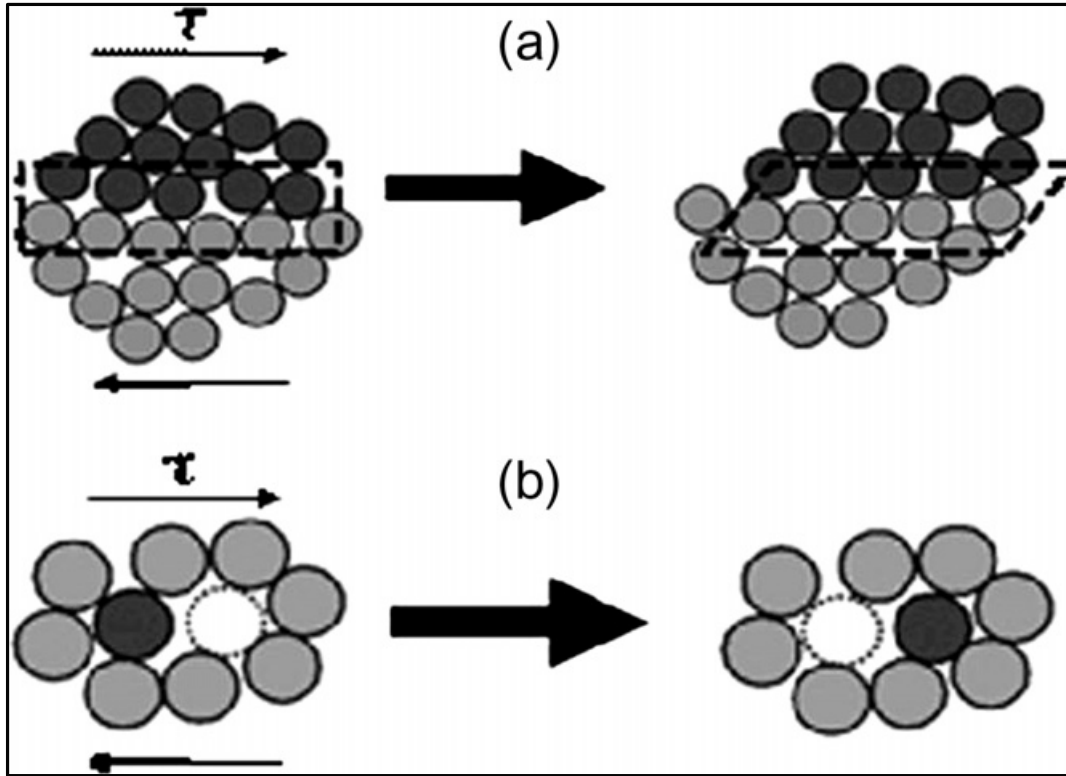


Figure 5.7 Deformation mechanism in metallic glasses: (a) Formation of shear band transformation zones and (b) Free Volume Model. [70]

From earlier studies, we notice that metallic glasses hold very high strength, hardness and elastic modulus values. Therefore, in order to study the mechanical behavior of $\text{Co}_{72}\text{B}_{19.2}\text{Si}_{4.8}\text{Cr}_4$, $\text{Co}_{64.8}\text{Fe}_{7.2}\text{B}_{19.2}\text{Si}_{4.8}\text{Cr}_4$, $\text{Co}_{57.6}\text{Fe}_{14.4}\text{B}_{19.2}\text{Si}_{4.8}\text{Cr}_4$, and $\text{Co}_{50.4}\text{Fe}_{21.6}\text{B}_{19.2}\text{Si}_{4.8}\text{Cr}_4$ alloys, hardness and elastic modulus have been evaluated by performing nano-indentation. Using a berkovich tip and applying a maximum load of 7000 μN , hardness and elastic modulus of the four alloy compositions was estimated. It was found that the hardness and elastic modulus of these four compositions fall in the range 14.20 GPa – 12.20 GPa and 180.20 GPa – 116.23 GPa. Figure 5.6 shows the load vs displacement curves and Table 5.1, gives the corresponding hardness and elastic modulus values for all the alloy compositions.

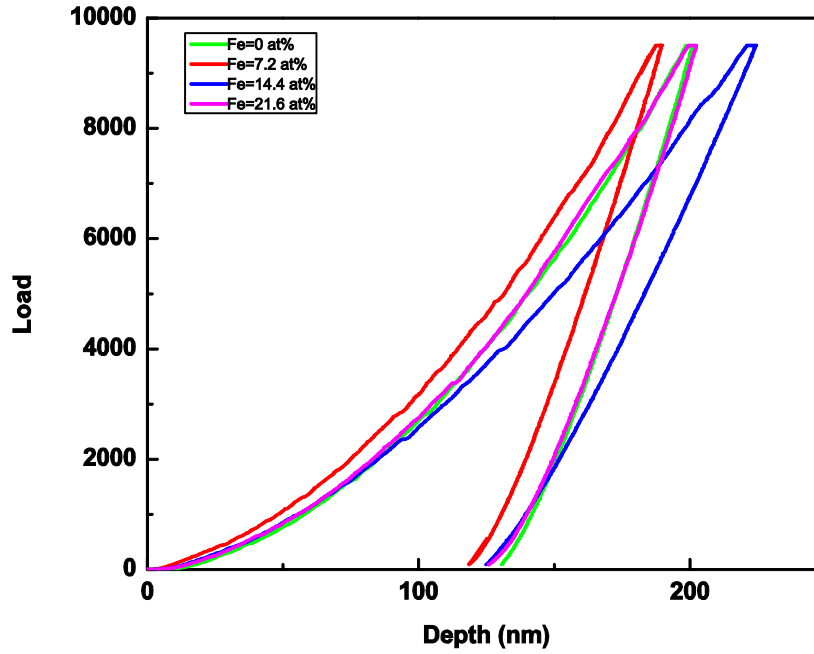


Figure 5.8 Load vs displacement for the alloys $\text{Co}_{72}\text{B}_{19.2}\text{Si}_{4.8}\text{Cr}_4$, $\text{Co}_{64.8}\text{Fe}_{7.2}\text{B}_{19.2}\text{Si}_{4.8}\text{Cr}_4$, $\text{Co}_{57.6}\text{Fe}_{14.4}\text{B}_{19.2}\text{Si}_{4.8}\text{Cr}_4$, and $\text{Co}_{50.4}\text{Fe}_{21.6}\text{B}_{19.2}\text{Si}_{4.8}\text{Cr}_4$.

Table 5.1 Mechanical properties such as hardness and elastic modulus of Co-Fe ribbons.

Composition	Iron concentration (at%)	Hardness (Gpa)	Elastic Modulus (GPa)
$\text{Co}_{72}\text{B}_{19.2}\text{Si}_{4.8}\text{Cr}_4$	0	13.41	174.6
$\text{Co}_{64.8}\text{Fe}_{7.2}\text{B}_{19.2}\text{Si}_{4.8}\text{Cr}_4$	7.2	14.20	180.20
$\text{Co}_{57.6}\text{Fe}_{14.4}\text{B}_{19.2}\text{Si}_{4.8}\text{Cr}_4$	14.4	12.20	116.23
$\text{Co}_{50.4}\text{Fe}_{21.6}\text{B}_{19.2}\text{Si}_{4.8}\text{Cr}_4$	21.6	12.40	157.21

CHAPTER 6

CONCLUSIONS

The present work focuses on the evaluation of three main characteristics – glass forming ability, magnetic properties and mechanical behavior of ferromagnetic iron and cobalt based metallic glasses. Magnetic properties of the system $[\{ \text{Co}_{(1-X)}\text{Fe}_{(X)} \}(0.75) \text{B}(0.2)\text{Si}(0.05)]_{96}\text{Cr}_4$, where $X = 0, 0.1, 0.2$, and 0.3 has been extensively studied. Correlation of glass forming ability and magnetic properties has successfully explained the magnetic properties of the varied compositions in the Co-Fe system. It has been observed that increased interaction of ferromagnetic elements with non-magnetic metalloids leads to deterioration of magnetic properties of the composition.

The amorphous alloy compositions were found to be extremely soft magnetic. However, few heat treatment steps were employed in order to enhance their magnetic properties. Heating the amorphous materials to a temperature above the crystallization event for each of the alloys has improved the saturation magnetization of the composition while the coercivity could not be maintained as low as that obtained in amorphous alloys. Amongst the four compositions, the alloy $\text{Co}_{72}\text{B}_{19.2}\text{Si}_{4.8}\text{Cr}_4$ showed a two peak crystallization event. Hence, by annealing at the intermediate peak temperatures, saturation magnetization similar to the fully crystalline samples could be attained with a compromise on coercivity values. However, the annealed samples fall in the category of semi-hard magnetic materials.

Using a metallic glass precursor, coatings with a composite structure leading to a hardness higher than the substrate can be obtained. Highly catalytic nano-crystalline structural morphology can be obtained for iron based metallic glass powder using high power ball milling. Evaluation of hardness on nano scale for the melt spun amorphous compositions have shown

exceptionally high values. Excellent magnetic and mechanical behavior has been observed for the alloy system $[\{ \text{Co}_{(1-x)}\text{Fe}_{(x)} \} (0.75) \text{B}(0.2)\text{Si}(0.05)]_{96}\text{Cr}_4$.

BIBLIOGRAPHY

- [1] W. Wang, C. Dong and C. Shek. Bulk metallic glasses. *Materials Science and Engineering: R: Reports* 44(2), pp. 45-89. 2004.
- [2] C. Suryanarayana and A. Inoue. *Bulk Metallic Glasses* 2011.
- [3] Y. Zhang, H. Tan and Y. Li. Bulk glass formation of 12 mm rod in La–Cu–Ni–Al alloys. *Materials Science and Engineering: A* 375pp. 436-439. 2004.
- [4] A. Inoue, T. Zhang and T. Masumoto. Al–La–Ni amorphous alloys with a wide supercooled liquid region. *Mater. Trans. JIM* 30(12), pp. 965-972. 1989.
- [5] J. F. Löffler. Bulk metallic glasses. *Intermetallics* 11(6), pp. 529-540. 2003.
- [6] A. Peker and W. L. Johnson. A highly processable metallic glass: $Zr_{41.2}Ti_{13.8}Cu_{12.5}Ni_{10.0}Be_{22.5}$. *Appl. Phys. Lett.* 63(17), pp. 2342-2344. 1993.
- [7] D. Turnbull. Phase changes. *Solid State Physics* 3pp. 225-306. 1956.
- [8] D. Turnbull. Under what conditions can a glass be formed? *Contemporary Physics* 10(5), pp. 473-488. 1969.
- [9] Z. Lu and C. Liu. Glass formation criterion for various glass-forming systems. *Phys. Rev. Lett.* 91(11), pp. 115505. 2003.
- [10] Z. Lu and C. Liu. Glass formation criterion for various glass-forming systems. *Phys. Rev. Lett.* 91(11), pp. 115505. 2003.
- [11] R. W. Cahn. *Glasses and Amorphous Materials* 19919.
- [12] H. Bhadeshia and R. Honeycombe. *Steels: Microstructure and Properties: Microstructure and Properties* 2011.
- [13] W. L. Johnson. Bulk glass-forming metallic alloys: Science and technology. *MRS Bull* 24(10), pp. 42-56. 1999.
- [14] W. Wang, J. Lewandowski and A. Greer. Understanding the glass-forming ability of $Cu_{50}Zr_{50}$ alloys in terms of a metastable eutectic. *J. Mater. Res.* 20(09), pp. 2307-2313. 2005.
- [15] A. Inoue. Bulk amorphous alloys: Preparation and fundamental characteristics, vol. 4. *Trans Tech Publications Inc., Stafa-Zurich, Switzerland* 1998.
- [16] A. Inoue. Recent progress of Zr-based bulk amorphous alloys. 1996.
- [17] N. Nishiyama, K. Takenaka and A. Inoue. $Pd_{30}Pt_{17.5}Cu_{32.5}P_{20}$ alloy with low critical cooling rate of 0.067 K/s. *Appl. Phys. Lett.* 88(12), pp. 121908. 2006.

- [18] Y. Zhang, Y. Li, H. Tan, G. Chen and H. Davies. Glass forming ability criteria for La–Al–(Cu, Ni) alloys. *J. Non Cryst. Solids* 352(52), pp. 5482-5486. 2006.
- [19] A. Inoue, T. Nakamura, T. Sugita, T. Zhang and T. Masumoto. Bulky La-Al-TM (TM= transition metal) amorphous alloys with high tensile strength produced by a high-pressure die casting method. *Materials Transactions, JIM(Japan)* 34(4), pp. 351-358. 1993.
- [20] B. Giessen, J. Hong, L. Kabecoff, D. Polk, R. Raman and R. S. Amand. Compositional dependence of the thermal stability and related properties of metallic glasses I: T (g) for $\text{Ca}_{0.65}\text{M}_{0.35}$ and $\text{Zr}_{0.475}\text{Cu}_{0.475}\text{M}_{0.05}$ glasses', rapidly quenched metals III. Presented at Proc. 3 Rd International Conference on Rapidly Quenched Metals, Brighton, England. 1978.
- [21] H. Chen. Glass temperature, formation and stability of Fe, Co, Ni, Pd and Pt based glasses. *Materials Science and Engineering* 23(2), pp. 151-154. 1976.
- [22] S. Guo and C. T. LIU. Phase stability in high entropy alloys: Formation of solid-solution phase or amorphous phase. *Progress in Natural Science: Materials International* 21(6), pp. 433-446. 2011.
- [23] A. Takeuchi and A. Inoue. Calculations of mixing enthalpy and mismatch entropy for ternary amorphous alloys. *Materials Transactions-JIM* 41(11), pp. 1372-1378. 2000.
- [24] O. Gutfleisch, M. A. Willard, E. Brück, C. H. Chen, S. Sankar and J. P. Liu. Magnetic materials and devices for the 21st century: Stronger, lighter, and more energy efficient. *Adv Mater* 23(7), pp. 821-842. 2011.
- [25] A. Inoue, T. Zhang, W. Zhang and A. Takeuchi. Bulk nd-fe-al amorphous alloys with hard magnetic properties. *Materials Transactions, JIM (Japan)* 37(2), pp. 99-108. 1996.
- [26] P. Duwez and S. Lin. Amorphous ferromagnetic phase in iron-carbon-phosphorus alloys. *J. Appl. Phys.* 38(10), pp. 4096-4097. 1967.
- [27] A. Makino, T. Kubota, C. Chang, M. Makabe and A. Inoue. FeSiBP bulk metallic glasses with unusual combination of high magnetization and high glass-forming ability. *Materials Transactions* 48(11), pp. 3024-3027. 2007.
- [28] T. Bitoh, A. Makino and A. Inoue. Magnetization process and coercivity of Fe-(Al, Ga)-(P, C, B, Si) soft magnetic glassy alloys. *Materials Transactions* 45(4), pp. 1219-1227. 2004.
- [29] C. Chang, T. Kubota, A. Makino and A. Inoue. Synthesis of ferromagnetic Fe-based bulk glassy alloys in the Fe–Si–B–P–C system. *J. Alloys Compounds* 473(1), pp. 368-372. 2009.
- [30] Z. Gercsi, F. Mazaleyrat, S. Kane and L. Varga. Magnetic and structural study of $(\text{Fe}_{1-x}\text{Co}_x)_{62}\text{Nb}_8\text{B}_{30}$ bulk amorphous alloys. *Materials Science and Engineering: A* 375pp. 1048-1052. 2004.

- [31] A. Inoue, B. Shen, H. Koshiba, H. Kato and A. Yavari. Ultra-high strength above 5000 MPa and soft magnetic properties of Co–Fe–Ta–B bulk glassy alloys. *Acta Materialia* 52(6), pp. 1631-1637. 2004.
- [32] A. Inoue and R. E. Park. Soft magnetic properties and wide supercooled liquid region of Fe-P-B-Si base amorphous alloys. *Materials Transactions, JIM (Japan)* 37(11), pp. 1715-1721. 1996.
- [33] A. Inoue and B. L. Shen. A new Fe-based bulk glassy alloy with outstanding mechanical properties. *Adv Mater* 16(23-24), pp. 2189-2192. 2004.
- [34] A. Inoue and B. Shen. Formation and soft magnetic properties of Co-Fe-Si-B-Nb bulk glassy alloys. *Materials Transactions* 43(5), pp. 1230-1234. 2002.
- [35] A. Inoue and B. Shen. Soft magnetic bulk glassy Fe-B-Si-Nb alloys with high saturation magnetization above 1.5 T. *Materials Transactions* 43(4), pp. 766-769. 2002.
- [36] A. Inoue, T. Zhang, T. Itoi and A. Takeuchi. New Fe-Co-Ni-Zr-B amorphous alloys with wide supercooled liquid regions and good soft magnetic properties. *Mater. Trans. JIM* 38(4), pp. 359-362. 1997.
- [37] A. Makino, T. Kubota, C. Chang, M. Makabe and A. Inoue. FeSiBP bulk metallic glasses with unusual combination of high magnetization and high glass-forming ability. *Materials Transactions* 48(11), pp. 3024-3027. 2007.
- [38] M. Miglierini, R. Vittek and M. Hasiak. Impact of annealing temperature on magnetic microstructure of Fe₈₀Zr₄Ti₃Cu₁B₁₂ rapidly quenched alloy. *Materials Science and Engineering: A* 449pp. 419-422. 2007.
- [39] M. Miglierini, R. Vittek and M. Hasiak. Impact of annealing temperature on magnetic microstructure of Fe₈₀Zr₄Ti₃Cu₁B₁₂ rapidly quenched alloy. *Materials Science and Engineering: A* 449pp. 419-422. 2007.
- [40] A. Mitra, H. Kim, B. Shen, N. Nishiyama and A. Inoue. Crystallization and magnetic properties of Fe₄₀Co₄₀Cu_{0.5}Al₂Zr₉Si₄B_{4.5} and Fe₆₂Co_{9.5}Gd_{3.5}Si₁₀B₁₅ amorphous alloys. *Materials Transactions* 44(8), pp. 1562-1565. 2003.
- [41] B. Shen, C. Chang and A. Inoue. Formation, ductile deformation behavior and soft-magnetic properties of (Fe, Co, Ni)–B–Si–Nb bulk glassy alloys. *Intermetallics* 15(1), pp. 9-16. 2007.
- [42] B. Shen and A. Inoue. Bulk glassy Fe-Ga-P-C-B-Si alloys with high glass-forming ability, high saturation magnetization and good soft magnetic properties. *Materials Transactions* 43(5), pp. 1235-1239. 2002.
- [43] B. Shen, H. Koshiba, A. Inoue, H. Kimura and T. Mizushima. Bulk glassy Co₄₃Fe₂₀Ta_{5.5}B_{31.5} alloy with high glass-forming ability and good soft magnetic properties. *Materials Transactions-JIM* 42(10), pp. 2136-2139. 2001.

- [44] N. Sulitanu, F. Brînză and F. Tufescu. Effect of Co substitution for ni on the microstructure and magnetic properties of (Fe, Ni)-based amorphous alloys produced by melt spinning. *J. Non Cryst. Solids* 351(5), pp. 418-425. 2005.
- [45] W. Zhang, Y. Long, M. Imafuku and A. Inoue. Thermal stability and soft magnetic properties of (Fe, Co)-(Nd, Dy)-B glassy alloys with high boron concentrations. *Materials Transactions* 43(8), pp. 1974-1978. 2002.
- [46] B. Shen, M. Akiba and A. Inoue. Effects of si and mo additions on glass-forming in FeGaPCB bulk glassy alloys with high saturation magnetization. *Physical Review B* 73(10), pp. 104204. 2006.
- [47] A. Inoue and B. Shen. Soft magnetic bulk glassy Fe-B-Si-Nb alloys with high saturation magnetization above 1.5 T. *Materials Transactions* 43(4), pp. 766-769. 2002.
- [48] Y. Yoshizawa, S. Oguma and K. Yamauchi. New Fe-based soft magnetic alloys composed of ultrafine grain structure. *J. Appl. Phys.* 64(10), pp. 6044-6046. 1988.
- [49] A. Inoue and B. Shen. Soft magnetic properties of nanocrystalline Fe-Co-B-Si-Nb-Cu alloys in ribbon and bulk forms. *J. Mater. Res.* 18(12), pp. 2799-2806. 2003.
- [50] V. Ponnambalam, S. J. Poon and G. J. Shiflet. Fe-based bulk metallic glasses with diameter thickness larger than one centimeter. *J. Mater. Res.* 19(05), pp. 1320-1323. 2004.
- [51] T. Zhang, F. Liu, S. Pang and R. Li. Ductile fe-based bulk metallic glass with good soft-magnetic properties. *Materials Transactions* 48(5), pp. 1157. 2007.
- [52] C. Schuh and T. Nieh. A nanoindentation study of serrated flow in bulk metallic glasses. *Acta Materialia* 51(1), pp. 87-99. 2003.
- [53] H. Hilzinger. Applications of metallic glasses in the electronics industry. 1985.
- [54] K. Mohri. Review on recent advances in the field of amorphous-metal sensors and transducers. *Magnetics, IEEE Transactions on* 20(5), pp. 942-947. 1984.
- [55] K. Shimamura, Y. Matsumoto and T. Matsunaga. Some applications of amorphous alloy coatings by sputtering. *Surface and Coatings Technology* 50(2), pp. 127-133. 1992.
- [56] G. Kumar, A. Desai and J. Schroers. Bulk metallic glass: The smaller the better. *Adv Mater* 23(4), pp. 461-476. 2011.
- [57] W. C. Oliver and G. M. Pharr. Measurement of hardness and elastic modulus by instrumented indentation: Advances in understanding and refinements to methodology. *J. Mater. Res.* 19(01), pp. 3-20. 2004.

- [58] A. Takeuchi and A. Inoue. Classification of bulk metallic glasses by atomic size difference, heat of mixing and period of constituent elements and its application to characterization of the main alloying element. *Materials Transactions* 46(12), pp. 2817-2829. 2005.
- [59] J. Kudrnovský, N. Christensen and O. Andersen. Electronic structures and magnetic moments of $\text{Fe}_{3-y}\text{Si}_{1-y}$ and $\text{Fe}_{3-x}\text{V}_x\text{Si}$ alloys with DO_3 -derived structure. *Physical Review B* 43(7), pp. 5924. 1991.
- [60] H. Kronmüller. Theory of the coercive field in amorphous ferromagnetic alloys. *J Magn Magn Mater* 24(2), pp. 159-167. 1981.
- [61] P. Mohn. The calculated electronic and magnetic properties of the tetragonal transition-metal semi-borides. *Journal of Physics C: Solid State Physics* 21(15), pp. 2841. 1988.
- [62] Y. Liu, Y. Wang, L. Xiao, D. Song, Y. Wang, L. Jiao and H. Yuan. Structure and electrochemical behaviors of a series of Co–B alloys. *Electrochim. Acta* 53(5), pp. 2265-2271. 2008.
- [63] G. Zhou and H. Bakker. Atomically disordered nanocrystalline Co_2Si by high-energy ball milling. *Journal of Physics: Condensed Matter* 6(22), pp. 4043. 1994.
- [64] M. Trudeau, J. Huot, R. Schulz, D. Dussault, A. Van Neste and G. L'Espérance. Nanocrystalline Fe-(Co, Ni)-Si-B: The mechanical crystallization of amorphous alloys and the effects on electrocatalytic reactions. *Physical Review B* 45(9), pp. 4626. 1992.
- [65] S. Das, A. Mukhopadhyay, S. Datta and D. Basu. Prospects of microwave processing: An overview. *Bull. Mater. Sci.* 32(1), pp. 1-13. 2009.
- [66] E. Thostenson and T. Chou. Microwave processing: Fundamentals and applications. *Composites Part A: Applied Science and Manufacturing* 30(9), pp. 1055-1071. 1999.
- [67] Z. Zhenfang, Z. Liangchi and M. Yiu-Wing. Modelling friction and wear of scratching ceramic particle-reinforced metal composites. *Wear* 176(2), pp. 231-237. 1994.
- [68] Y. Cheng and E. Ma. Atomic-level structure and structure–property relationship in metallic glasses. *Progress in Materials Science* 56(4), pp. 379-473. 2011.
- [69] A. Argon. Plastic deformation in metallic glasses. *Acta Metallurgica* 27(1), pp. 47-58. 1979.
- [70] M. M. Trexler and N. N. Thadhani. Mechanical properties of bulk metallic glasses. *Progress in Materials Science* 55(8), pp. 759-839. 2010.